



NATIONAL CENTER FOR TRANSPORTATION SYSTEMS PRODUCTIVITY AND MANAGEMENT

Next-Generation Wireless Bridge Weigh-in-Motion (WIM) System Integrated with Nondestructive Evaluation (NDE) Capability for Transportation Infrastructure Safety

Contract # DTRT12GUTC12 with USDOT Office of the Assistant Secretary for Research and Technology (OST-R)
Final Report
May 2014

Principal Investigator: Yang Wang, PhD



National Center for Transportation Systems
Productivity and Management
O. Lamar Allen Sustainable Education Building
788 Atlantic Drive, Atlanta, GA 30332-0355
P: 404-894-2236 F: 404-894-2278
nctspm@ce.gatech.edu nctspm.gatech.edu



DISCLAIMER

The contents of this report reflect the views of the authors, who are responsible for the facts and the accuracy of the information presented herein. This document is disseminated under the sponsorship of the U.S. Department of Transportation's University Transportation Centers Program, in the interest of information exchange. The U.S. Government assumes no liability for the contents or use thereof.

1. Report No.:		2. Government Accession No.:		3. Recipient's Catalog No.:	
4. Title and Subtitle: : Next-Generation Wireless Bridge Weigh-in-Motion (WIM) System Integrated with Nondestructive Evaluation (NDE) Capability for Transportation Infrastructure Safety			5. Report Date: May 2014		
			6. Performing Organization Code:		
7. Author(s): Yang Wang, Nasim Uddin, Laurence J. Jacobs, Jin-Yeon Kim			8. Performing Organ. Report No.:		
9. Performing Organization Name and Address: School of Civil and Environmental Engineering, Georgia Institute of Technology, 790 Atlantic Dr NW Atlanta, GA 30332-0355			10. Work Unit No.:		
			11. Contract or Grant No.: RP 12-21		
12. Sponsoring Agency Name and Address: Georgia Department of Transportation Office of Materials & Research 15 Kennedy Drive Forest Park, GA 30297-2534			13. Type of Report and Period Covered: Final; 7/1/2012 - 5/15/2014		
			14. Sponsoring Agency Code:		
15. Supplementary Notes: N/A					
16. Abstract: This project seeks to develop a rapidly deployable, low-cost, and wireless system for bridge weigh-in-motion (BWIM) and nondestructive evaluation (NDE). The system is proposed to assist in monitoring transportation infrastructure safety, for the first time ever, in a two-fold approach: control of overloaded trucks and safety assessment/monitoring of transportation infrastructure. The system contains individual wireless sensing nodes that integrate state-of-the-art shear strain sensors suitable for concrete bridge components, and ultrasonic nondestructive evaluation (NDE) devices suitable for steel components.					
17. Key Words: Wireless sensors, bridge weigh in motion, nondestructive evaluation			18. Distribution Statement:		
19. Security Classification (of this report): Unclassified	20. Security Classification (of this page): Unclassified	21. Number of Pages: 74	22. Price:		

Form DOT 1700.7 (8-69)

TABLE OF CONTENTS

1	Executive Summary	1
2	Wireless Sensing System Development and Validation	3
2.1	Wireless Sensing System Development	3
2.1.1	<i>Remote Monitoring through Cellphone Network</i>	3
2.1.2	<i>Martlet Wireless Sensing Unit</i>	5
2.1.3	<i>Strain Gage Wing Board</i>	6
2.1.4	<i>Ultrasonic Wing Board</i>	8
2.1.5	<i>Smart ADC/DAC Wing Board</i>	10
2.1.6	<i>Integrated Accelerometer Wing</i>	13
2.2	Validation of Wireless Sensing System Development	14
2.2.1	<i>Validation of Martlet Strain Gage Wing Board</i>	15
2.2.1.1	Calibration test.....	15
2.2.1.2	Dynamic test	17
2.2.2	<i>Validation of Martlet Ultrasonic Wing Board</i>	19
2.2.3	<i>Validation of Martlet ADC/DAC and Integrated Accelerometer Wings</i>	21
2.3	Summary	24
3	Application of Diffuse Ultrasonic Technique for Crack Depth Measurement in Concrete	26
3.1	The Diffuse Ultrasonic Technique	26
3.1.1	<i>Generation of Diffuse Ultrasonic Field in Concrete</i>	26
3.1.2	<i>Experimental Setup and Procedure</i>	28
3.1.3	<i>Measurement on Arrival Time of Maximum Energy Density</i>	31
3.1.4	<i>Energy Velocity based Crack Determination via ATME</i>	33
3.2	Measurement on Cracks in Concrete Beams	34
3.2.1	<i>Concrete Beam Preparation and Crack Initiation</i>	34
3.2.2	<i>Diffuse Ultrasonic Measurements</i>	36
3.2.3	<i>Destructive Test (Core Results)</i>	39
3.2.4	<i>Comparisons and Summary of Results</i>	42

3.3	Summary	42
4	Bridge Weigh-in-Motion (BWIM) Analysis	45
4.1	Moving Force Identification (MFI) Method	46
4.2	Demonstration of the application of the MFI Method.....	48
4.2.1	<i>Derivation of Element Stiffness Matrix and Mass Matrix</i>	48
4.2.2	<i>Meshing of the Instrumented Bridge on Highway US-78.....</i>	49
4.2.3	<i>Selection of Moving Vehicles.....</i>	51
4.2.4	<i>Verification of the FE Model with Moving Vehicles.....</i>	52
4.2.5	<i>Field Testing of MFI with Full-Loaded 2-Axle Rigid Truck.....</i>	55
4.2.6	<i>Field Testing of MFI with Full-Loaded 5-Axle Semitrailer.....</i>	63
4.3	Summary	70
5	Summary and Discussion.....	73
6	Bibliography.....	75

1 Executive Summary

This project aims to deliver a rapidly deployable, low-cost, and wireless system for bridge weigh-in-motion (BWIM) and nondestructive evaluation (NDE). The system contains individual wireless sensing nodes that integrate state-of-the-art shear strain sensors suitable for concrete bridge components, and ultrasonic nondestructive evaluation (NDE) devices suitable for steel components. The result will be a transportation infrastructure monitoring and protection system that is highly portable, effective, and the operation will require little manpower. The main components of this system include: 1) a wireless sensing system for real-time data acquisition and online delivery; 2) tools for data analysis and interpretation; and 3) a database for storage and archival.

To achieve the research goals, wireless sensors (nodes) are developed to capture the real-time structural response of a bridge to actual traffic conditions. Combined with a sophisticated computer model of the bridge, the structural response data can be used to assess the gross weights and axle loadings of individual vehicles, essentially making the bridge a weighing scale. These BWIM data can then be used in a number of ways, including identifying and controlling overweight trucks.

Towards the NDE functionality, the wireless sensing node supports high-speed ultrasonic measurements for monitoring crack development on a bridge. Each wireless sensor node is capable of providing low amplitude, high-frequency (megahertz) excitations to the hot spot area of a bridge component. Tiny-amplitude vibration waves at a small neighborhood near the crack are, in turn, detected by the sensor node after traveling around the crack. These captured vibration signals can offer information on the

size and location of cracks within the structure. These NDE technologies can assist in monitoring crack or damage growth in critical structural members. Thus, this system can not only assist in monitoring and reducing overweight trucks, but also detect bridge damage caused by overload.

Traditionally, sensing systems required for both BWIM and NDE entail bulky equipment that is impractical to deploy sensing nodes in the field at high densities. Recent developments in electronics have enabled the research team, through judicious selection and assembly of commercial-off-the-shelf components, to develop a new generation of compact wireless sensing devices. Used in conjunction with solar panels, these devices should provide for both denser and lower cost sensor coverage without the requirement for providing electrical connections to the power grid. Aggregated by an on-site local gateway that communicates through cellphone networks, both BWIM and NDE data can be viewed in real time by DOT bridge engineers for close monitoring of bridge conditions.

The rest of this report is organized as follows. Section 2 describes the development and validation of a wireless sensing system, including the overall communication system over cellphone network and designs of individual wireless sensing nodes. Section 3 describes the diffuse ultrasonic technique for NDE application on concrete. Section 4 describes the bridge weigh motion analysis using strain data to be collected with wireless sensors. Section 5 provides a summary and discussion.

2 Wireless Sensing System Development and Validation

This chapter presents the development and validation of the wireless sensing system. Section 2.1 introduces the hardware development of the wireless sensing system, including system architecture of remote communication through cellphone network, and design of the individual wireless sensing nodes. In Section 2.2, the performance of the wireless sensing system is evaluated by both laboratory and field experiments.

2.1 Wireless Sensing System Development

This section describes the design and development of the wireless sensing system. The section first presents the communication architecture of the entire wireless system through cellphone network. Then, a newly developed wireless sensing node, named Martlet, is presented in the second part. Finally, the development of four Martlet accessory sensor boards is introduced. These include the ultrasonic, strain gage, general ADC/DAC (analog-to-digital conversion and digital-to-analog conversion), and integrated accelerometer boards.

2.1.1 Remote Monitoring through Cellphone Network

FIGURE 2.1 shows the communication diagram of the entire system for remote monitoring. A local gateway aggregates wireless sensor data from a bridge site, and the gateway is equipped with a cellular modem for data transmission over cellphone network.

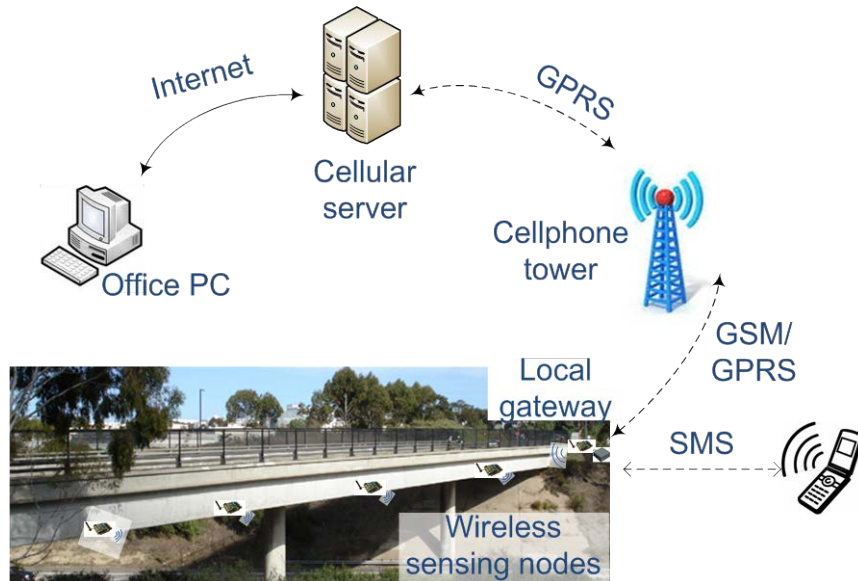


FIGURE 2.1

Bridge monitoring through cellphone network

As a result, the local gateway is first capable of local communication with the wireless nodes installed on the bridge through a low-power IEEE 820.15.4 wireless protocol [1]. The gateway also communicates with cellphones, as well as computers on the Internet. To initiate each data collection, a regular cellphone can send a short text message to wake up the local gateway. The through cellphone network, the local gateway sets up an Internet data connection with an office PC. Based on the command contained in the wake-up text message, the local gateway either requests experimental settings (such as sampling frequencies and time, data acquisition channels, etc.) from the office PC to conduct a new data collection, or sends the latest collected data to the office PC.

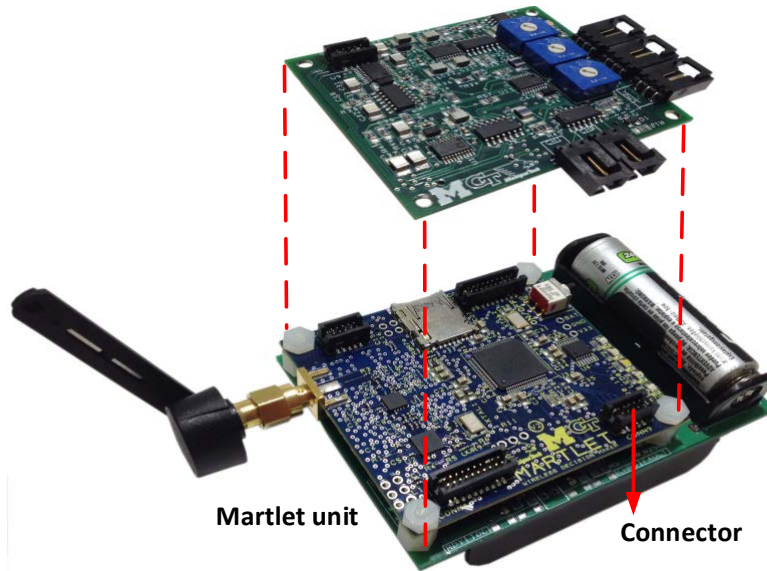


FIGURE 2.2

The Martlet wireless node (2.5in × 2.25in)

2.1.2 Martlet Wireless Sensing Unit

Martlet is a new-generation low-cost wireless sensing node developed for structural health monitoring purpose (FIGURE 2.2) [2]. The development of Martlet is a joint effort among the Laboratory for Intelligent Systems and Technologies at the University of Michigan, the Laboratory for Smart Structural Systems at Georgia Institute of Technology, and the Department of Civil and Environmental Engineering at Michigan Technological University. The Martlet wireless node adopts a Texas Instruments Piccolo microcontroller as its core processor, which runs at 80 MHz clock frequency.

The high clock frequency of the microcontroller enables Martlet to achieve high-frequency data acquisition and high-speed onboard computation. Another key feature of the Martlet node is its extensible hardware design, which allows the Martlet node to simultaneously collect data from multiple types of sensors through different accessory

sensor boards (termed “wing” boards). For large-quantity of long-term data acquisition, the data volume may exceed the capacity of microcontroller memory. In this case, a regular Micro SD card (like these used in digital cameras) can be plugged in to provide extra data storage. The data stored in the Micro SD card can be easily readable from a personal computer or transferred through wireless network. The Martlet node integrates a 2.4 GHz radio for local low-power wireless communication through IEEE 820.15.4 wireless protocol [1]. The local communication range can be up to 1,600 ft at line-of-sight, and the maximum wireless transfer rate can reach 250 kbps. The dimension of the Martlet node is 2.5 in. by 2.25 in.

2.1.3 Strain Gage Wing Board

In order to incorporate strain gage measurement into the Martlet wireless sensing system, a strain gage wing board is developed (FIGURE 2.3). The strain gage board is compatible with two types of commonly-used strain gages (120 Ω and 350 Ω). The functional diagram of the strain gage wing is shown in FIGURE 2.4, which consists of three major parts, i.e. a Wheatstone quarter bridge, signal amplification, and anti-aliasing filtering.

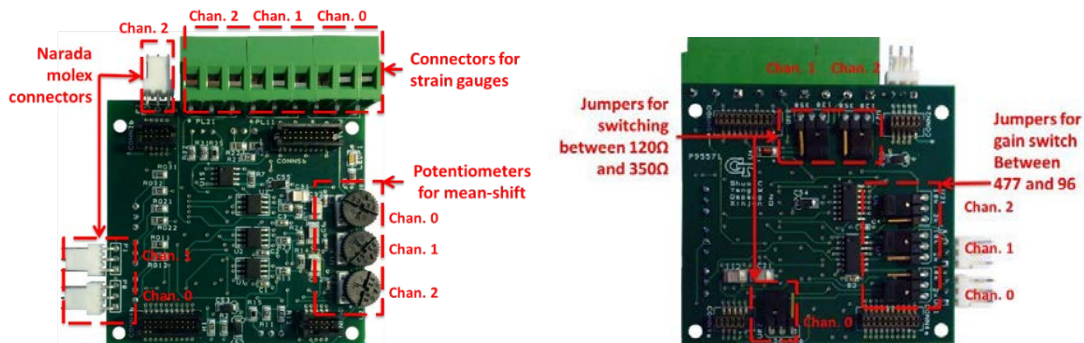


FIGURE 2.3

Strain gage wing board

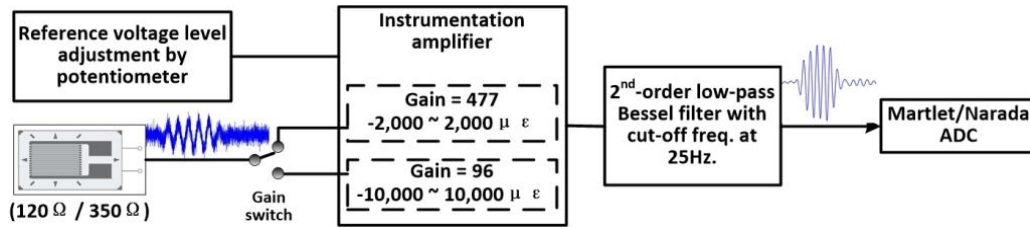


FIGURE 2.4

Functional diagram for one strain gage channel

The Wheatstone quarter bridge is used to measure the resistance value of the strain gage, which is represented by voltage signal (changing with strain) as output of the bridge circuit. One onboard jumper allows users to select the strain gage type (120 Ω or 350 Ω). Since the deformation of civil structures are usually small (e.g. at tens of microstrains), the variation in output voltage signal is very low and can be easily contaminated by electrical noise. To overcome this difficulty, an amplification circuit is designed to increase the signal-to-noise ratio. One instrumentation amplifier is adopted to amplify the signal.

Another onboard jumper allows users to select the gain factor ($\times 477$ or $\times 96$). The gain factor also determines the measurement range of the strain gage wing board, which is $\pm 2,000 \mu\epsilon$ for $\times 477$ amplification and $\pm 10,000 \mu\epsilon$ for $\times 96$ amplification. The other function of the instrumentation amplifier is to shift up the mean value of output voltage signal. In the designated zero-strain stage, by using a thumbwheel potentiometer, the voltage signal passing the instrumentation amplifier is shifted to the center of the analog-to-digital (ADC) range (i.e. 1.65 V) so as to achieve maximum measurement range for both positive and negative strain. The voltage signal at zero-strain stage (1.65 V) is termed as reference voltage. During the experiment, the voltage change with respect to the

reference voltage indicates the fluctuation of strain. Finally, the signal will go through an anti-aliasing filter with a cutoff frequency of 25 Hz further decrease noise contamination.

2.1.4 Ultrasonic Wing Board

Ultrasonic nondestructive evaluation (NDE) is widely used for detecting crack development in structures. The ultrasonic wing board (FIGURE 2.5) can be integrated with two ultrasonic transducers (one transmitting and one receiving) to effectively detect the crack size. FIGURE 2.6 shows the functional diagram of the ultrasonic wing boards, which consists of an excitation module and a receiving module.

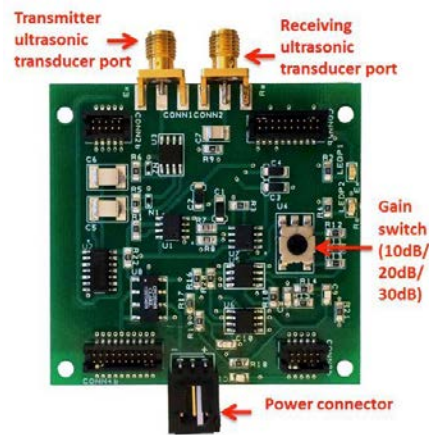


FIGURE 2.5

The Martlet ultrasonic wing board

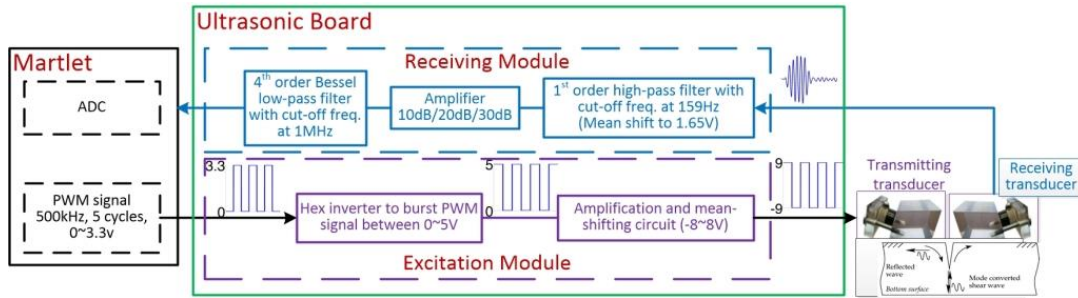


FIGURE 2.6

Functional diagram for ultrasonic wing board

The excitation module provides the input signal into the transmitting transducer for generating ultrasonic waves into the structure. The pulse-width module (PWM) of the Martlet node generates bursts containing five cycles of square-waves (0~3.3 V) at 500 kHz frequency. In order to provide high-amplitude excitation signal into the transmitting transducer, the excitation module amplifies the square-waves to ± 8 V without changing the frequency. The transmitting transducer converts the amplified electrical square-wave signals into a series of Rayleigh ultrasonic excitation waves which propagates into the specimen.

After the Rayleigh wave propagates along to specimen, the receiving transducer captures the response signal at the other side. The receiving module of the ultrasonic wing board consists of three main parts, mean-value shifting, signal amplification, and anti-alias filtering. The mean value of the output voltage signal is uplifted to the center of Martlet analog-to-digital conversion range (i.e. 1.65 V) so as to achieve the maximum measurement range for both positive and negative signals. Moreover, since the immediately received signal is of very low amplitude (~ 50 mV), the signal needs to be amplified in order to increase the signal-to-noise ratio. The gain factor of the

amplification module can be easily adjusted to 10 dB, 20 dB and 30 dB by a rotary switch. Finally, the received signal will be processed by an anti-aliasing filter before entering the analog-to-digital conversion module of Martlet node. The magnitude of the received signal usually decreases with the increase of the crack size, due to the characteristics of the ultrasonic Rayleigh wave propagation.

2.1.5 Smart ADC/DAC Wing Board

For generic purpose, Martlet is designed with the ability to convert various real-world measurands into digital signals, followed by the conversion of the results into real-world actions (i.e., actuation). Sensors are typically connected to the analog-to-digital conversion (ADC) module, and actuators are connected to the digital-to-analog conversion (DAC) module. To this end, the Martlet Smart ADC/DAC wing shown in FIGURE 2.7 was developed as a general purpose interface for sensing and actuation.

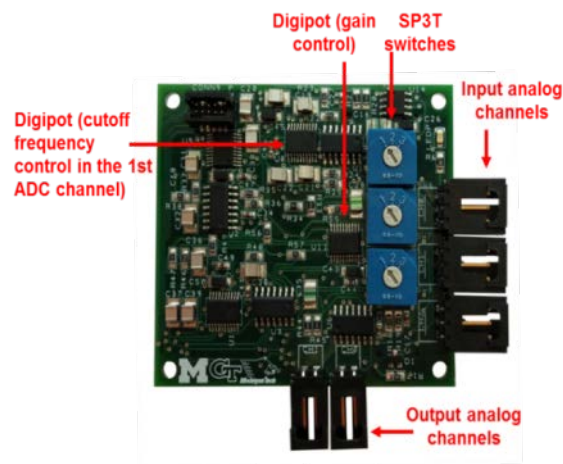


FIGURE 2.7

Smart ADC/DAC wing with components highlighted

For conditioning analog sensor (input) signals, the ADC/DAC board takes input from three analog sensors, supporting any commonly used transducer that outputs a 0 ~ 5 V signal and requires a 5 V power source. The functional diagram of the smart ADC/DAC wing is shown in FIGURE 2.8. Each channel contains three possible signal conditioning paths as schematically shown in FIGURE 2.8; the paths are selectable with a double-pole three-throw (DP3T) mechanical switch.

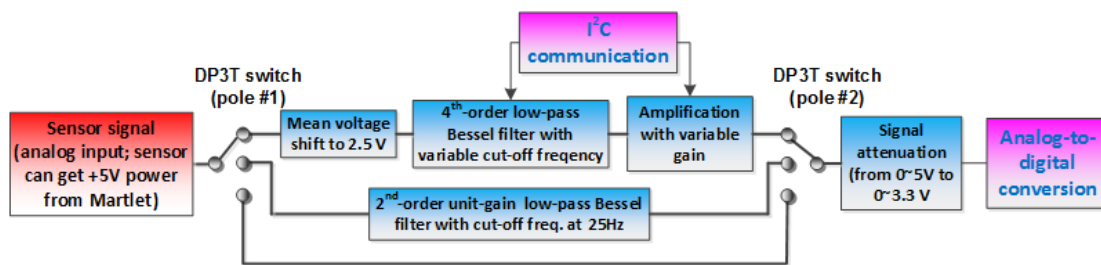


FIGURE 2.8

Functional diagram for an analog input channel

The first path offers the most sophisticated signal conditioning including mean shift, on-the-fly programmable low-pass filtering, and on-the-fly programmable amplification. The mean-shift ensures that the maximum dynamic range is possible by shifting mean value to the center of the input range of the following analog filter. The programmable low-pass filter (with cut-off frequencies from 15 Hz to a few hundred Hz) maximizes the spectrum of the captured signal while ensuring proper anti-aliasing. The programmable gain (with settings from $\times 1.9$ to $\times 190$) can be used to amplify the signal. An I²C signal from the Martlet is used to interface with factory-calibrated digitally controllable potentiometers to accurately adjust the gain and cutoff frequencies. The second path on the DP3T switch has a fixed gain of $\times 1$ and an anti-aliasing filter with a

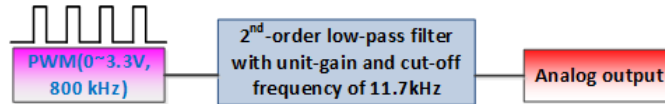


FIGURE 2.9

Functional diagram for an analog input channel.

cutoff frequency of 25 Hz. This path is most useful when simplicity is desired and the fixed-value gain and cutoff are appropriate. The third path passes the signal directly through to the Martlet ADC without amplification or filtering. This setting is used in conjunction with external signal conditioning. After the signal passes through one of the three paths it is scaled down from a maximum range of 5 V to a maximum range of 3.3 V. This is necessary so that the signal matches the input range of the Martlet's internal ADC.

For generating analog output signals, the ADC/DAC wing board contains two independent analog output channels. The functional diagram of each channel is shown in FIGURE 2.9. The DAC process begins with the Martlet's internal pulse width modulator (PWM) that is used to output a square wave. The output is then filtered to generate an analog signal. A 2nd-order low-pass filter with unity gain and a cutoff frequency of 11.7 kHz is used to remove the high-frequency components of the PWM signal, leaving only the low-frequency content as the analog output. The output range of each DAC channels is 0~3.3 V, and the settling time among different output voltage levels is around 60 μ s.

2.1.6 Integrated Accelerometer Wing

In order to obtain accurate acceleration measurement, and in the meantime reduce sensor cost, one solution is to integrate a low cost chip accelerometer and signal conditioner into a single PCB as shown in FIGURE 2.10. The integrated accelerometer board uses a tri-axial MEMS (micro-electro-mechanical-systems) accelerometer (STMicroelectronics LIS344ALH). A jumper on the PCB selects either a ± 2 g or ± 6 g measurement scale. The noise density of the measurement is $25 \mu\text{g}/\sqrt{\text{Hz}}$ along the x-axis and y-axis, and $50 \mu\text{g}/\sqrt{\text{Hz}}$ along the z-axis. The voltage signals from the accelerometer are conditioned using the same circuitry used in the first path of the Martlet Smart ADC/DAC wing from FIGURE 2.8. The mean-shifted adjustable filtering and gain enable the integrated accelerometer board to be used in any orientation and signal amplitude while allowing it to maintain an ideal dynamic range and spectrum of the sampled signal. The filter and gain settings are stored in nonvolatile memory on the PCB.

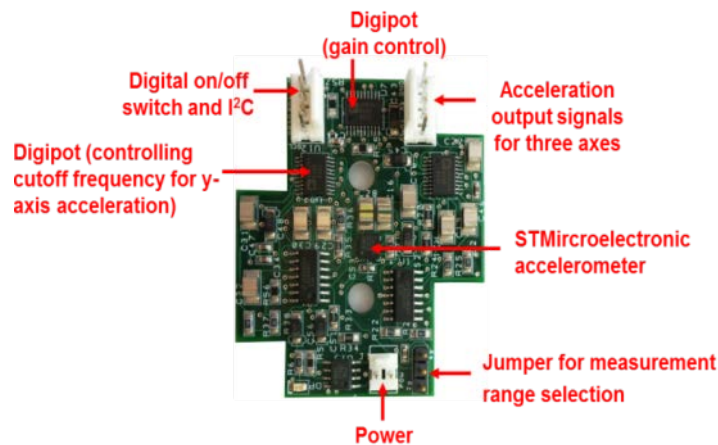


FIGURE 2.10

Integrated accelerometer board

The integrated accelerometer board is placed in a compact weatherproof enclosure with a dimension of 2.28 in × 2.52 in × 1.38 in as shown in FIGURE 2.11. In this case, the wing is not actually attached to the Martlet base. Rather, the integrated accelerometer board is connected to the Martlet node with an eight-wire cable. Three wires in the cable are allocated for the acceleration output signals (X, Y and Z channels), two are allocated for I²C communications, one is allocated for power, one is allocated for ground, and the last one is allocated to a digital signal that allows the Martlet base board to power the accelerometer wing on and off. The current draw of the integrated accelerometer board is ~12 mA (referenced at 3.3 V) under normal working conditions and ~1 μA when switched off.



FIGURE 2.11

Weather-proof package of the integrated accelerometer

2.2 Validation of Wireless Sensing System Development

In order to evaluate the performance of the Martlet wireless node and the associated wing boards, both laboratory and field experiments are conducted. A calibration test and a dynamic experiment are carried out with the strain gage wing to test the accuracy and

stability of the sensor board. Moreover, the ultrasonic wing is tested with a notch specimen to evaluate its sensitivity to the crack depth. The ADC/DAC and integrated accelerometer wings are compared with a high-precision cabled accelerometer during a field experiment.

2.2.1 Validation of Martlet Strain Gage Wing Board

In order to validate the performance of the strain gage wing board, two experiments are carried out. The first test calibrates the strain gage wing board with the strain calibration box, and the second test verifies the dynamic performance of the strain gage wing board.

2.2.1.1 Calibration test

The calibration test evaluates the accuracy and noise level of the strain gage wing board. The layout of the test is shown in FIGURE 2.12. In the calibration test, the quarter bridge setting of a commercial strain calibration box is used to assess the measurement accuracy. In this test, four scenarios of strain gage wing board are tested. Each scenario is a combination of strain gage type and measurement range, including $120 \Omega + 2,000 \mu\epsilon$ range, $120 \Omega + 10,000 \mu\epsilon$ range, $350 \Omega + 2,000 \mu\epsilon$ range, and $350 \Omega + 10,000 \mu\epsilon$ range.

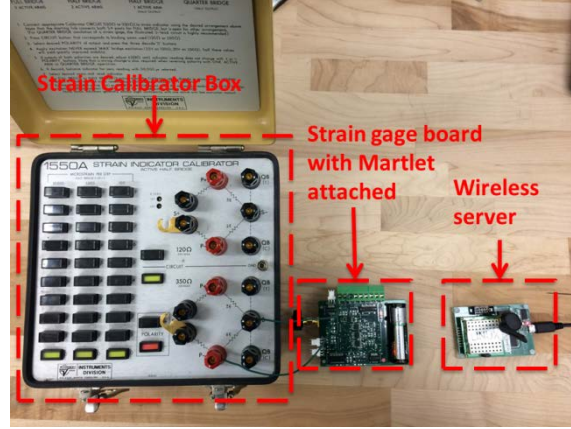


FIGURE 2.12

Experimental setup for the calibration test of the strain gage wing board

FIGURE 2.13 plots the strain level measured by Martlet strain gage board against the benchmark strain level provided by the commercial calibration box. A close match is observed between two sets of strain data. Linear regression is performed between the two strain data sets, for each test scenario. The linear regression plots demonstrate a high linearity between measurement and benchmark values.

The noise level in each test scenario is estimated by the standard deviation value based on Eq. (2.1).

$$\text{STD} = \sqrt{\frac{1}{N-1} \sum_{i=1}^N (\Delta\varepsilon_i)^2} \quad (2.1)$$

where, $\Delta\varepsilon_i$ denotes the difference between the measured strain and the benchmark strain at the i^{th} strain level; N is the total number of strain levels. Particularly for the two scenarios with $2,000 \mu\varepsilon$, the noise level is only slight over $1 \mu\varepsilon$, showing a performance comparable to cabled strain measurement systems. Overall, the calibration test demonstrates that the strain gage wing board can accurately capture strain gage data.

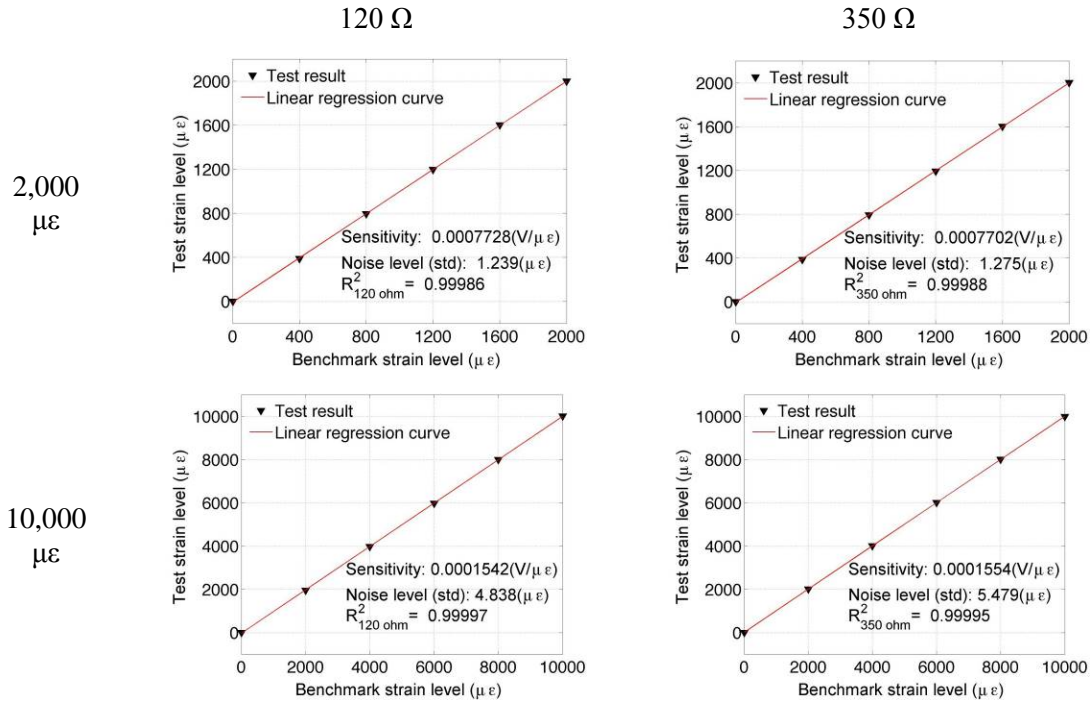


FIGURE 2.13

Strain data calculated from strain gage wing board

2.2.1.2 Dynamic test

FIGURE 2.14 shows the experimental setup for the dynamic test of the strain gage wing board. In the experiment, two strain gages are installed on the same side of a compact-tension specimen. Strain gage 1 is placed near the initial crack and strain gage 2 is placed in the middle of the specimen. The strain gages are connected directly with strain gage wing board, with measurement range set as 10,000 με. The specimen is installed on a tensile testing machine, which provides 5 Hz sinusoidal load with peak to peak values as 0.1 ~ 3 kips. The sampling frequency is 1,000 Hz.

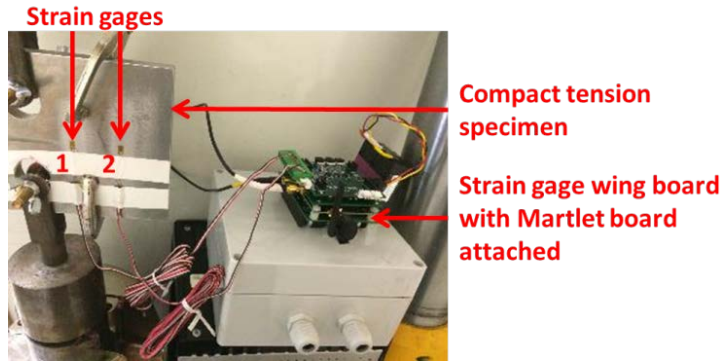


FIGURE 2.14

Experiment setup for dynamic test of strain gage wing board

FIGURE 2.15 (a) plots part of the received signals from two strain gages. The frequency spectra are shown in FIGURE 2.15 (b). The red line and blue line represent the signals from the strain gage 1 and strain gage 2, respectively. Because strain gage 2 is near the bending axis, the gage experiences much less strain. The figures show that the dynamic strain signal matches cycling loading applied to the specimen. Moreover, the resonance frequency shown in the frequency spectrum is the same as the cyclic loading frequency. Therefore, the dynamic experiment demonstrates that the strain gage wing can perform reliably under dynamic loading conditions.

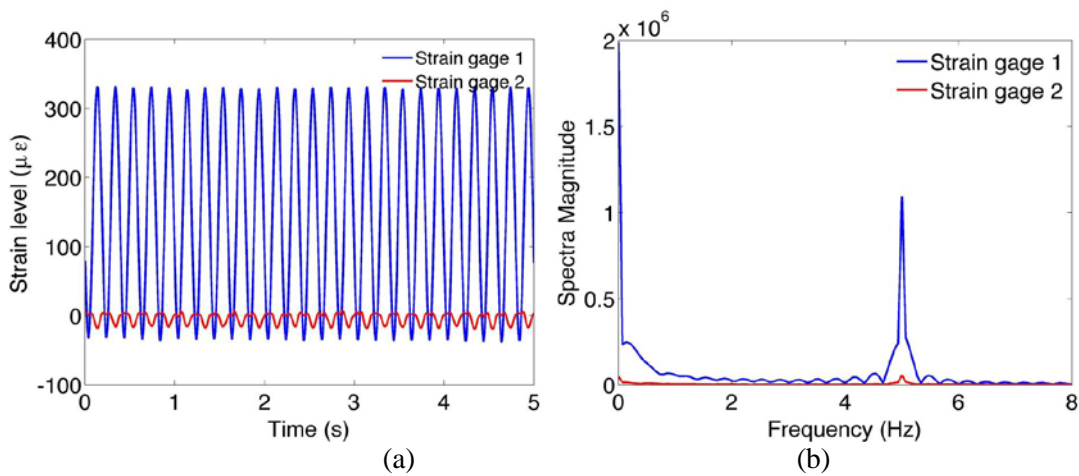


FIGURE 2.15

Strain data collected from strain gage wing board

2.2.2 Validation of Martlet Ultrasonic Wing Board

In order to evaluate the sensitivity of the ultrasonic wing board to crack size, an experiment is carried out on a steel specimen (FIGURE 2.16). There are four existing notches of different depths on the specimen surface, to simulate different levels of cracks. Ultrasonic transmitting-receiving data is collected on undamaged surface and then across all four notches using the two wedge transducers. The high-speed microcontroller in the Martlet node enables high frequency data acquisition. During the experiment, the sampling frequency and time are set to be 2 MHz and 16 ms, respectively.

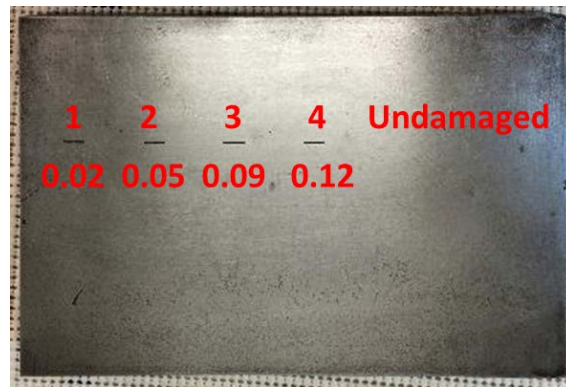


FIGURE 2.16

Photo of the test specimen with notches with depths shown (unit: inch)

The received signals are reconstructed from the sampling frequency 2 MHz to 200 MHz. Red line in FIGURE 2.17 shows received signal for 61 ultrasonic bursts, each burst containing five cycles at 500 kHz and lasting 260 μ s. Blue line in the figure shows reconstructed signal, which illustrates that the signal reconstruction process can restore more authentic amplitude.

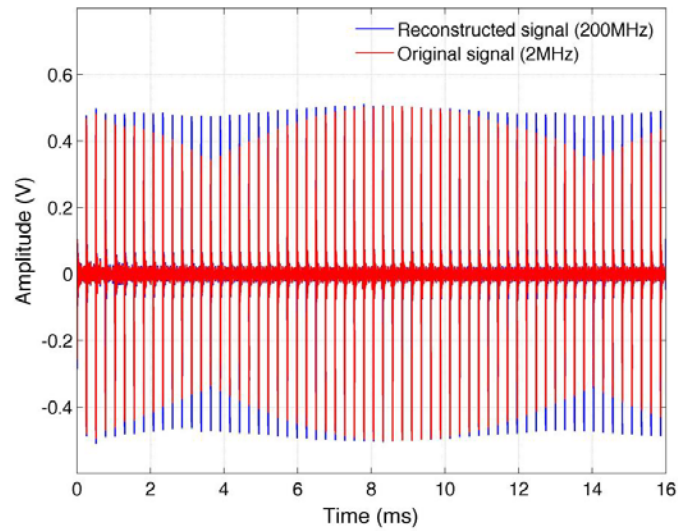


FIGURE 2.17

Comparison between original and reconstructed signals

In order to accurately capture the amplitude of received signals, the Hilbert–Huang transform (HHT) is selected to calculate the envelope of received single burst. One example of the reconstructed signal and its envelope at undamaged position is shown in FIGURE 2.18.

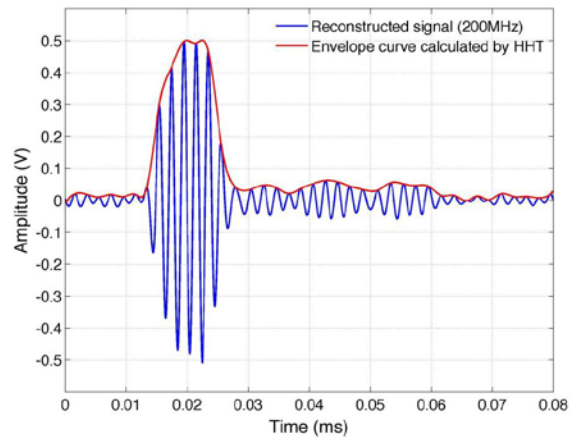


FIGURE 2.18

Example for one burst of signal and envelope curve at undamaged position

FIGURE 2.19 plots the envelope maximum of the received signals with respect to the notch depth. For each notch depth, the magnitude value is taken as the envelope maximum averaged from 61 bursts. Experimental results indicated that the amplitude decreases when the depth increases. The experiment demonstrates that the ultrasonic wing board is sensitive to surface defects, and thus can be used for damage assessment.

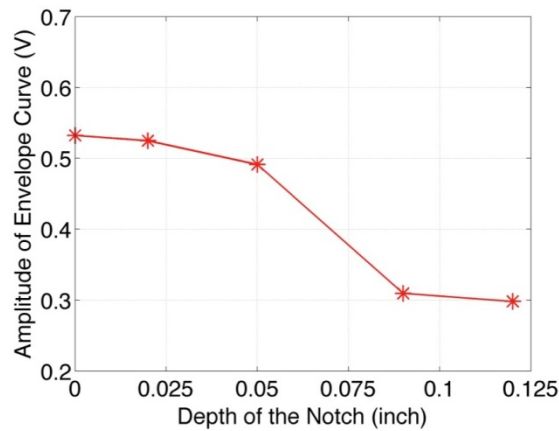


FIGURE 2.19

Average envelope maximum at different notches

2.2.3 Validation of Martlet ADC/DAC and Integrated Accelerometer Wings

To validate the field performance of Martlet ADC/DAC and integrated accelerometer wings, experiments are conducted on a two-story, two-bay concrete frame structure on Georgia Tech campus. FIGURE 2.20 illustrates the instrumentation plan of the experiment. One integrated accelerometer wing is installed at the middle joint of first second elevated slab, and the other at the second elevated slab. In addition, one ADC/DAC wing is installed at each of the two ends of second elevated slab. Each ADC/DAC wing obtains acceleration signal through a commercial MEMS accelerometer

(Silicon Designs 2012-002). In the meantime, four high-precision cabled force-balance accelerometers (Kinematics EpiSensor ES-T) are placed side-by-side at each of the four wireless sensor locations as reference. Both cabled and wireless sensors measure the acceleration along the longitudinal direction of the frame structure. A modal shaker is installed at the middle joint of the second elevated slab to apply dynamic load to the frame along the longitudinal direction.

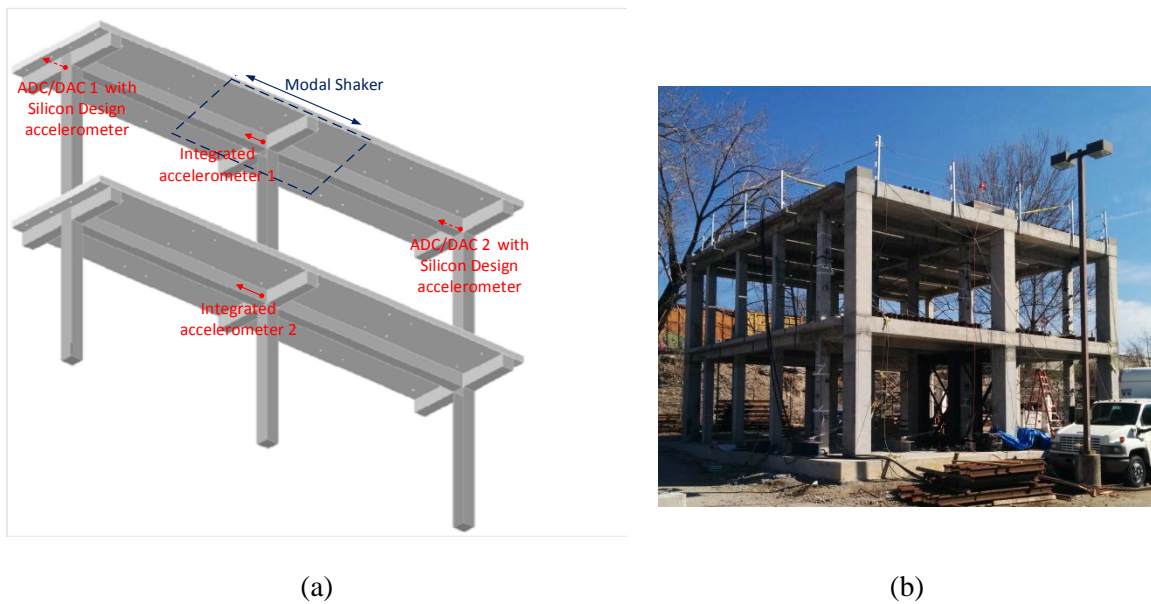


FIGURE 2.20

Experiment instrumentation plan

FIGURE 2.21 compares the synchronized time history data from the cabled force-balance accelerometer and the Martlet integrated accelerometer wing. The left two plots show the data over 25 seconds, and the right plots are close-up view of 6 seconds. The structural response is measured when the modal shaker applies a scaled El Centro excitation to the frame structure.

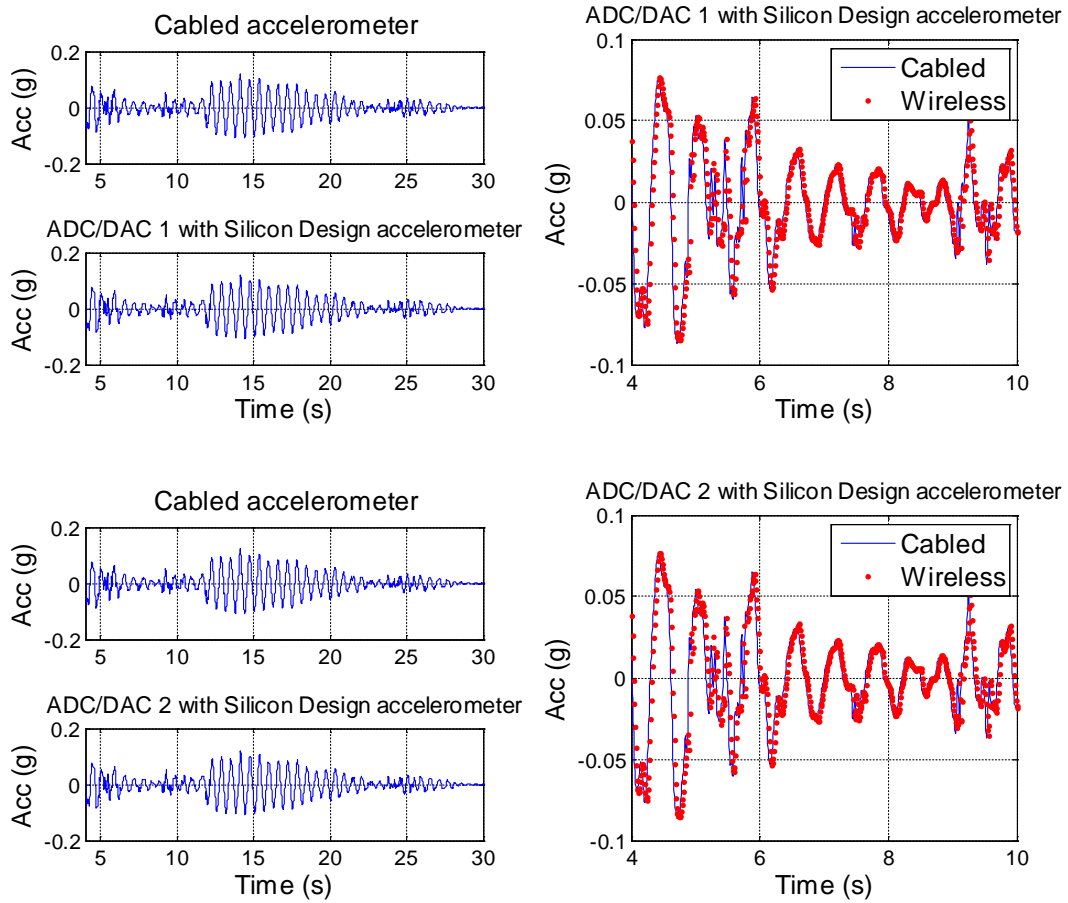


FIGURE 2.21

Comparison between cabled accelerometer and ADC/DAC wing (with a MEMS accelerometer)

FIGURE 2.22 shows the synchronized time history data during the same excitation. The figure compares data from the cabled force-balance accelerometer and the Martlet ADC/DAC wing with Silicon Designs 2012-002 accelerometer. Again, the left two plots show the data over 25 seconds, and the right plots are close-up view of 6 seconds.

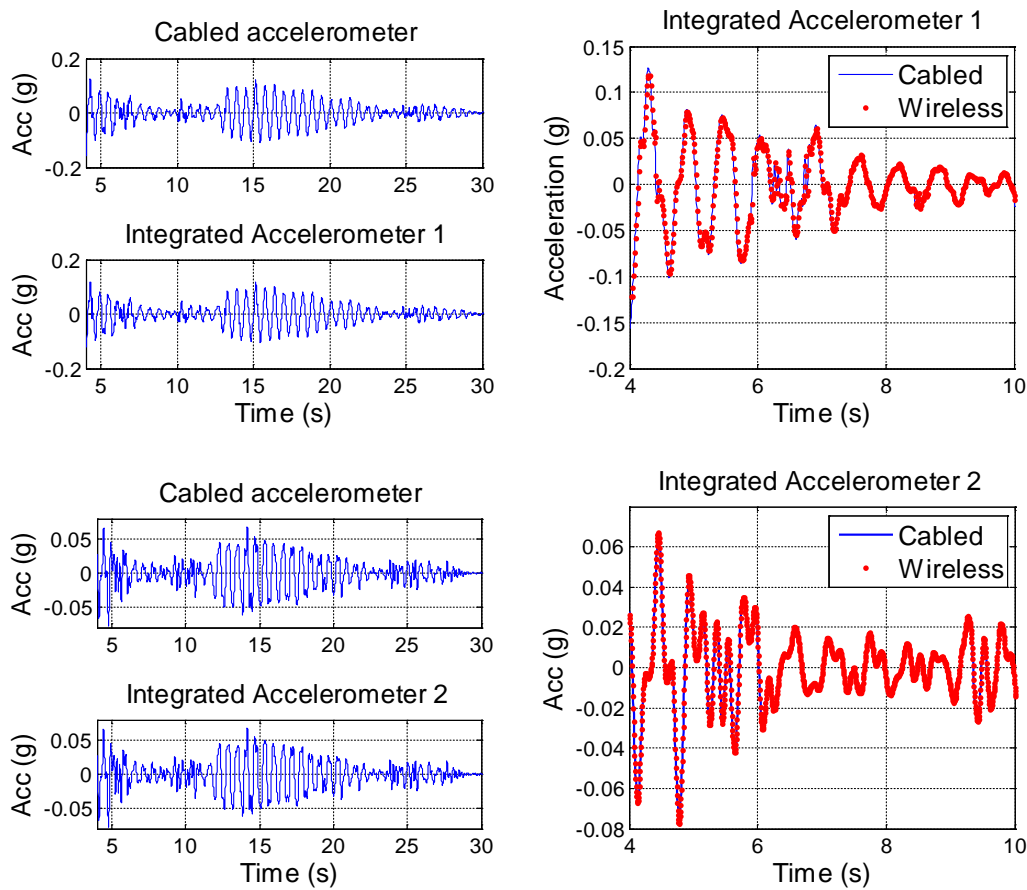


FIGURE 2.22

Comparison between cabled accelerometer and integrated accelerometer wing

In the experiment, the gain factor of the ADC/DAC and integrated accelerometer wings is set to 20 times, and the cutoff frequency is set as 25 Hz. The close agreement between the cabled and wireless data can be observed in all the plots, which indicates that the performance of wireless sensors is highly reliable.

2.3 Summary

This chapter presents the development and validation of the wireless sensing system. Cellphone network is adopted to transmit experiment data from the local gateway (on

bridge site) to an office computer. The bridge site can be deployed with multiple wireless sensing nodes named Martlet. The Martlet node is an extensible wireless platform which is able to execute high-frequency data acquisition and high-speed onboard computation. Standardized wing boards can be easily integrated with the Martlet node, which allows simultaneous data acquisition from multiple sensors of various types. Moreover, the onboard SD card significantly extends the data storage space of the Martlet node.

The Martlet strain gage wing can accurately measure both static and dynamic strain value of the 120 Ω and 350 Ω strain gage. The Martlet ultrasonic wing integrated with ultrasonic transducers can be used to effectively detect crack growth. The integrated accelerometer wing provided an economical and portable solution for acceleration measurement. In addition, for general sensor interfacing, the Martlet smart ADC/DAC wing can be used for pre-processing analog sensor signals before entering the onboard ADC. Both ADC/DAC and integrated accelerometer wings can change the gain factor and cutoff frequency of onboard signal conditioning on the fly.

The validation results demonstrate that the strain gage wing performs accurately and reliably in both static calibration and dynamic experiment. The achieved accuracy is sufficient for strain data needed in BWIM analysis. The ultrasonic NDE results using a notched specimen indicate that the ultrasonic wing is sensitive to the depth of the crack on the specimen. In addition, both the integrated accelerometer wing and the ADC/DAC connected with a commercial MEMS accelerometer can perform comparably with the high-precision cabled force-balance accelerometer.

3 Application of Diffuse Ultrasonic Technique for Crack Depth Measurement in Concrete

This chapter presents development of the diffuse ultrasonic technique that is applied to measure crack depths in real concrete beam specimens. Comparisons with other techniques including dye penetration and impact each technique are also shown. Finally the diffuse ultrasonic results are validated by comparing those from destructive core results. The results demonstrate high accuracy and robustness of the diffuse ultrasonic technique in measuring the crack depth in concrete.

3.1 The Diffuse Ultrasonic Technique

This section gives precise descriptions on measurement aspects of the diffuse ultrasonic technique including the method to generate and detect diffuse ultrasonic signals in concrete, experimental setup, data processing procedure to extract the arrival time of maximum energy (ATME) and diffusivity, and finally a way to determine crack depth based on measured ATME. It is also noted that a separate reference measurement needs to be performed on an uncracked location to obtain the diffuse ultrasonic material properties of the concrete that contains cracks under concern.

3.1.1 Generation of Diffuse Ultrasonic Field in Concrete

The transmitter and receiver used in this research are Ultrason WC 50 and Ultrason GC 500-D13 500 kHz broadband transducers with a diameter of 0.5 in. It should be noted that the diffuse field will converge to zero if it is averaged over random configurations or averaged in a finite volume, which is called phase cancellation [3], because of the fact

that diffuse wave is spatially and temporarily incoherent with the incident coherent signal and its rapid spatial fluctuation in phase and amplitude. Hence it is inevitable to design transducers with a small surface area to avoid phase cancellation in measurement of the diffuse field.

For this purpose, a small cone is designed and manufactured. The bottom diameter of the cone is 0.2 in, the top diameter is 0.08 in, its thickness 0.09 in. The cone is manufactured out of aluminum. The cone is attached with glue (LOCTITE Super Glue) to the center of the receiving transducer. FIGURE 3.1 shows a picture of a pair of transducers where the attached cone is clearly seen. Unfortunately, the added cone makes the transducer difficult to perfectly perpendicular to the surface, also to improve the consistent coupling conditions, a small clamp is accommodated to its fixture as shown in FIGURE 3.2. In all measurements, the separation distance is 2.4 in and the transducers are also placed far away from the specimen edges in order to avoid any possible edge effects.



FIGURE 3.1

Transmitter and receiver



FIGURE 3.2

Accommodated clamp with transducers

3.1.2 Experimental Setup and Procedure

A high voltage pulse generator (Panametrics 5058 PR) is used to provide the source signal of 400 V which is sufficient for energy transmission into the concrete samples. In order to get a high signal-to-noise ratio (SNR) from the concrete samples, a pre-amplifier (DigitalWave DW 2040G/A) – which amplifies the received signal by 40 dB – is used in series with a signal conditioning amplifier DigitalWave DW FTM 4000, which allows for an additional amplification of 20 dB. The amplifier also allows for setting a lowpass and highpass filter. They are set to their respective minimum (20 kHz) and maximum (4 MHz) values. A schematic layout of the ultrasonic diffusion experimental setup is shown in FIGURE 3.3. A four channel digital Tektronix TDS 5034 B oscilloscope is used for this research. All measured signals are sampled with a sampling frequency f_s of 50 MHz, recorded with 200000 record points, and then averaged 1000 times to obtain the signal to be processed. The impedance is always set to 1 M Ω . The oscilloscope runs Windows 2000 as an operating system and allows saving the acquired waveforms in the *.dat

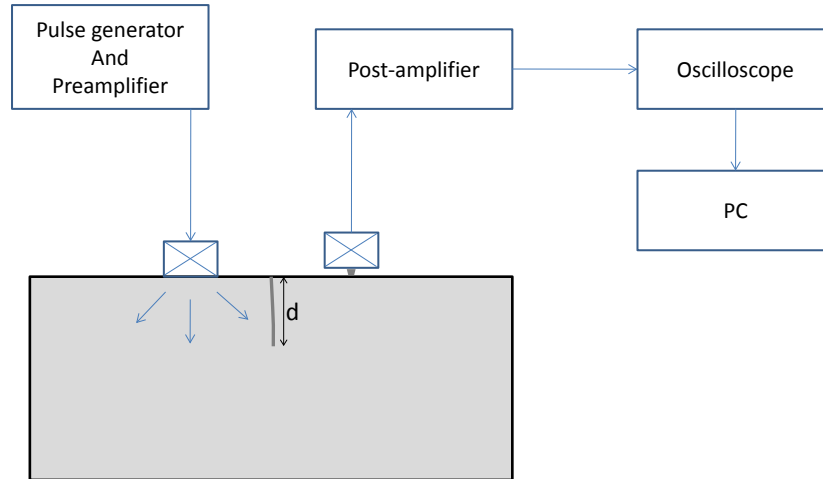


FIGURE 3.3

Schematic layout of the ultrasonic diffusion experimental setup

format which is readable by MATLAB. The files can be easily transferred to a PC using a flash drive for further signal processing. A viscous couplant is used to couple both of the transducers to the specimen.

A time-frequency analysis with the following main steps is performed to calculate the measured spectral energy density $\langle E(x, t, f) \rangle$ at a center frequency f (and at the measurement point x). A typical time signal is shown in FIGURE 3.4 that is used as an example in the following sections.

1. Divide the time signal into overlapping time windows of length Δt . The window length is set to $\Delta t = 15 \mu s$ and window overlap of 90% between consecutive windows is applied. Multiply the signal of each time window with the Hanning window to smooth the signal edges. The Hanning window gives signal outside of the window center less weight, so the overlap makes sure that the whole time-domain signal is taken into account for the further calculations. More time points are available if the windows overlap more.

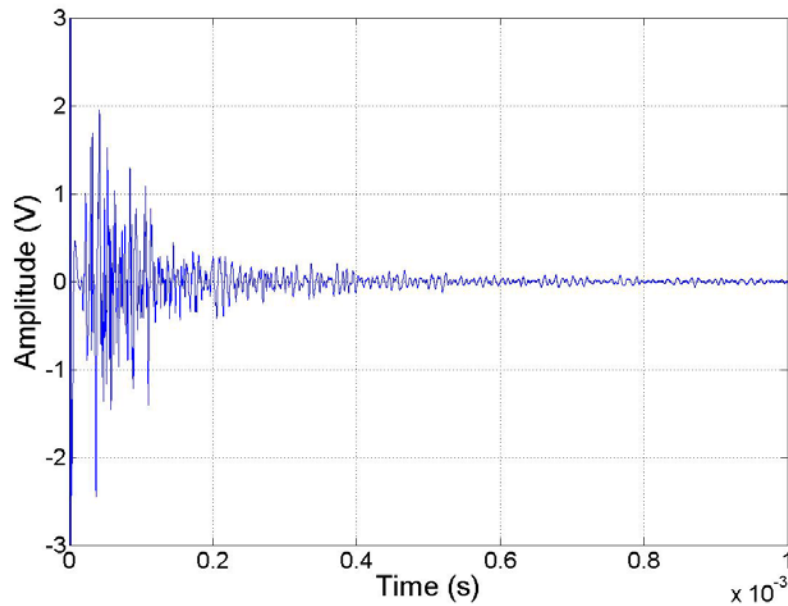


FIGURE 3.4

Typical diffuse ultrasonic signal

2. Calculate the discrete-time Fourier transform (DTFT) of each individual time window and square it. All the steps until here are done automatically by the Matlab function spectrogram which gives the resulting quantity from these three steps – the power spectral density – as one of its outputs. The power spectral density is basically a table of Fourier transforms for every time window centered at the center time of each time window.
3. Determine the spectral energy density of each time window in a certain frequency band by integrating the power spectral density in that bandwidth with width Δf centered around frequency f_c . The value used for this research is $\Delta f = 100$ kHz.

4. Construct a table of spectral energy density values that are assigned to discrete time points. The time points are centered in their respective time windows (centering assumes that the statistical signal properties like power spectrum are stationary over the length of the time window).

The resulting quantity denoted with $\langle E(x, t, f) \rangle$. $\langle E(x, t, f) \rangle$ is not the ultrasonic spectral energy density itself, but differs from that by a factor related to transducer sensitivity and a factor relating the measured local mean-square motions detected by the transducer to the local strain and kinetic energy densities. That factor is unknown, but presumed constant [4].

To recover the model parameters (P_0 , D and σ) from the experimentally determined spectral energy density $\langle E(x, t, f_c) \rangle$ (calculated for a frequency band with center frequency f_c), the energy density curve is fit to the approximate two-dimensional model [5]. Only data on a limited time range in which the energy density is clearly above noise level can be considered for the curve fit. The MATLAB function `lsqnonlin` is used for the curve fitting procedure. It must be noted that the indices of the infinite series of solution of 2-D model in [6] are selected to $n = m = 250$, which is determined by convergence test for Sufficient accuracy of the analytical solution [7].

3.1.3 Measurement on Arrival Time of Maximum Energy Density

Experiments are first conducted on the uncracked concrete sample to recover the diffusivity and dissipation coefficients of the hardened concrete. A typical time-frequency analysis and curve fitting described in the previous section are performed on the measured ultrasonic signals to retrieve diffusion parameters. FIGURE 3.5 shows the

experimental spectral energy density corresponding to the time signal shown in FIGURE 3.4, together with its fitted model on the logarithmic scale. The recovered diffuse parameters at 500 kHz of typical concrete are 15500 in²/s and 21000 s⁻¹ [8]. These parameters will be used in the numerical simulations to determine the diffuse energy velocity.

The experiments on the cracked specimens are essentially identical to those on the uncracked one. Transducers are placed 1.18 in off on both sides of the crack. FIGURE 3.6 shows the measured ultrasonic waveform for the specimen with a 4 in crack depth. In comparison with the result from uncracked sample (FIGURE 3.4), the delay of the pick arrival time is clearly seen (in this case $\Delta t = 30 \mu\text{s}$). This delay is due to the fact that the crack causes the energy propagation path to be longer, and hence will take more time to reach the receiver; this also makes the effective diffusivity D lower. The delay in diffuse energy (the peak) is affected by the absence of diffuse energy transfer across the crack.

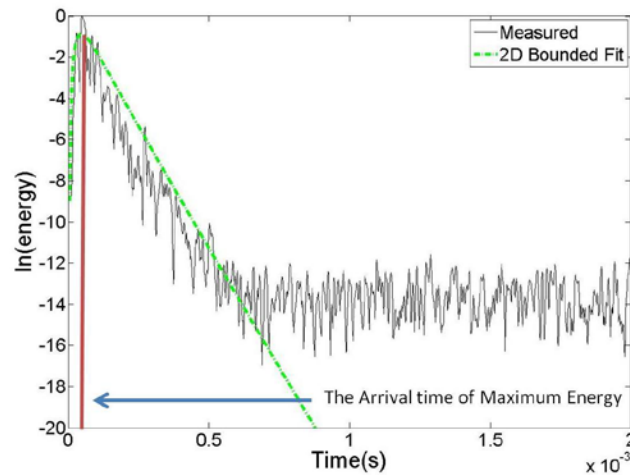


FIGURE 3.5

Energy density curve and curve fitting in uncracked sample

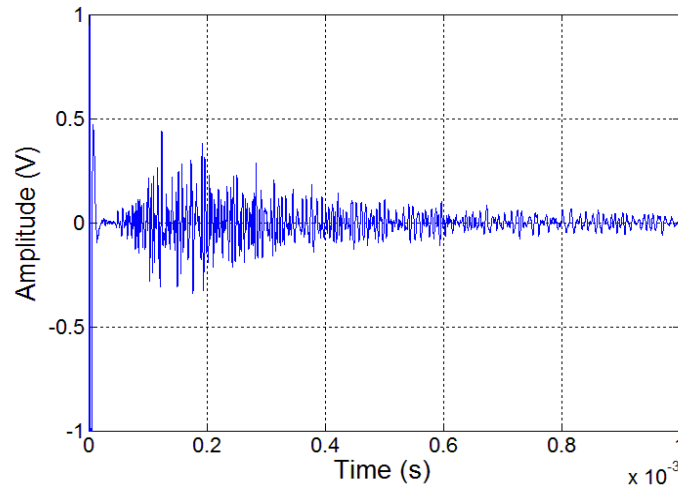


FIGURE 3.6

Diffuse ultrasound signal in 4 in cracked specimen

3.1.4 Energy Velocity based Crack Determination via ATME

In this section, an approach is developed and utilized to estimate vertical crack depth in concrete. It is based on diffused energy velocity. According to Seher, et al. [5], diffused energy velocity depends on the frequency (i.e. the diffusion parameters) and it is reported that there is an approximately linear relationship between the minimum propagation distance and the peak energy arrival time and diffused energy velocity at 500 kHz of their specimens is approximately 35917.3 in/s for the diffusion parameters (diffusivity: 15500 in²/s and dissipation: 21000 s⁻¹). Thus, based on this assumption, the ATME can be calculated from this known velocity and shortest propagation path of diffuse wave for each vertical crack depth. The crack depth can be calculated using the following equation:

$$t_{ATME} \cdot v_E = 2\sqrt{d^2 + (l_s / 2)^2} \quad (3.1)$$

where t_{ATME} is the ATME, v_E is the diffuse energy velocity, d is the crack depth and l_s is the source to receiver distance. Therefore, once the ATME is obtained from an experimental energy evolution curve, crack depth can be inferred from this energy velocity based method.

3.2 Measurement on Cracks in Concrete Beams

For measurements of crack depths in a situation closest to the real-world concrete structures, the team designed and prepared concrete beam specimens with steel reinforcement bars, in such a way that crack depths are controlled by the load is applied in three point bending. The cracking experiments are performed. Once cracks are generated different methods are applied to measure the crack depths. Finally comparisons are made to conclude the section.

3.2.1 Concrete Beam Preparation and Crack Initiation

Three reinforced concrete beams are cast to create real surface breaking cracks. Three beams, 94.5 in in length with a 10.0 in \times 6.0 in cross-section, contain two identically sized steel reinforcement bars (or rebars) placed at 1.3 in from the tension surface as seen in FIGURE 3.7. The rebar sizes of #6, #7, and #8 are used to promote a range of crack depths. Given the size of each beam, hand mixing the necessary concrete is not feasible, so donated concrete from Vulcan Concrete of Atlanta is used. Unfortunately, since the donated concrete is from another job site that had spare concrete, little is known about the

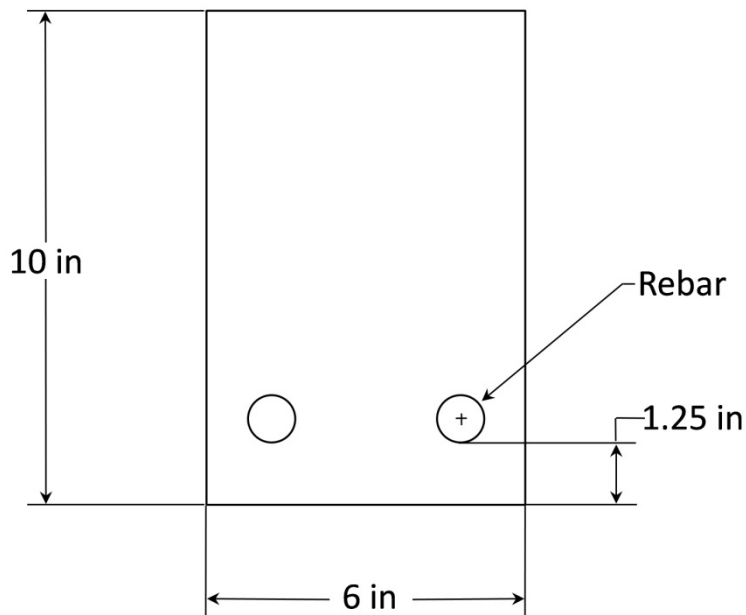


FIGURE 3.7

Cross section of beams

composition of the concrete mix itself. However, it is known that the concrete mix contains a maximum aggregate of #57 stone. Cylinders cast at the same time as the beams are tested in accordance with ASTM standards to measure a compressive strength of 3.6 ksi.

The beams are allowed to cure for 28 days before the surface is ground for testing. The beams are cracked in 4-point bending as seen in FIGURE 3.8. This set up results in evenly spaced cracks on each beam as can be seen in FIGURE 3.9. Ultrasonic testing is then conducted on the cracks after unloading. In addition, following the ultrasonic measurements, the crack depth was estimated using the average of the visible depths on either side of the beam.

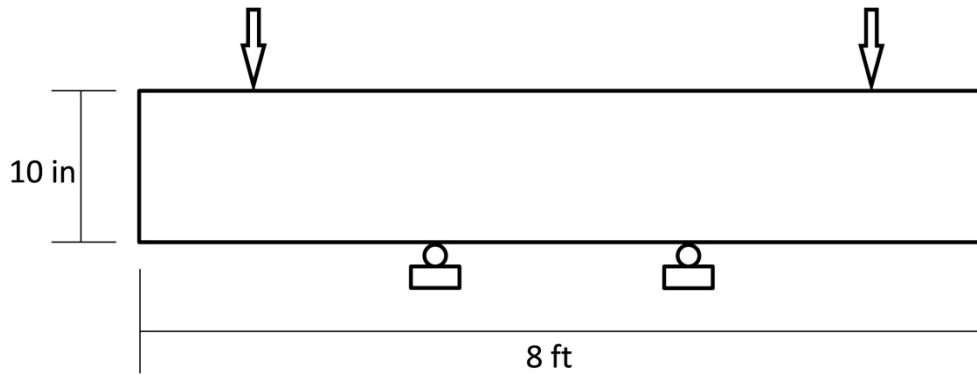


FIGURE 3.8
Four point bending setup



FIGURE 3.9
Flexural cracks

3.2.2 Diffuse Ultrasonic Measurements

First, diffuse measurements are performed on three different beams before each beam is loaded to recover the diffusivity and dissipation parameters. TABLE 3.1 shows the recovered diffuse parameters at 500 kHz for each concrete beam. These parameters were then used in the numerical simulations (using the FEA code developed in [5]) to calculate diffuse energy velocity and predict the peak arrival time for different crack depths.

First beam (A) is loaded up to 11500 lb, but second and third Beams (B and C) are loaded up to 10000 lb, and then all diffuse measurements are performed to estimate the depth of real cracks formed on each beam via 4 point bending after all beams are fully unloaded. Note that a 0.2 in deep artificial notch was created to promote crack growth in the middle of beam B. The ultrasonic experiments on the cracked specimens are essentially identical to those on the uncracked one, but conducted at a different location. Transducers are placed 1.2 in off on both sides of the crack. Also, FE simulation is conducted with the retrieved parameters for each beam and dimensions of concrete beam used for these simulations are tabulated in TABLE 3.2.

All cracks are estimated according to diffuse energy velocity based method explained in Section 3.1.

TABLE 3.3 shows diffuse energy speed for each beam. From these calculated diffuse energy speed and the shortest propagation path of diffuse wave, the theoretical ATME

TABLE 3.1
Diffusivity and dissipation parameters at 500 kHz for each concrete beam

Parameter	Diffusivity D	Dissipation σ
Beam A	15500 in ² /s	21000 s ⁻¹
Beam B	7750 in ² /s	21500 s ⁻¹
Beam C	12400 m ² /s	23000 s ⁻¹

TABLE 3.2
Dimensions of concrete beam

Parameter	Height	Width
Dimension	10.0 in	94.5 in

curve as a function of crack depth is calculated.

TABLE 3.3

Diffuse energy velocity for each beam

	Beam A	Beam B	Beam C
Energy speed [in/s]	35906	26496	34646

Therefore, once the ATME is obtained from an experimental energy evolution curve, crack depth can be inferred from this energy velocity based method. FIGURE 3.10, FIGURE 3.11 and FIGURE 3.12 show the results of crack depth estimation from the three different experiments. Note that the artificial notch is estimated almost correctly as 0.24 in.

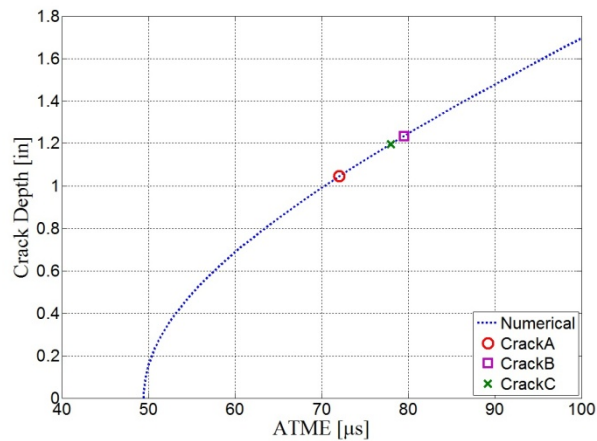


FIGURE 3.10

Crack depth estimation for Beam A

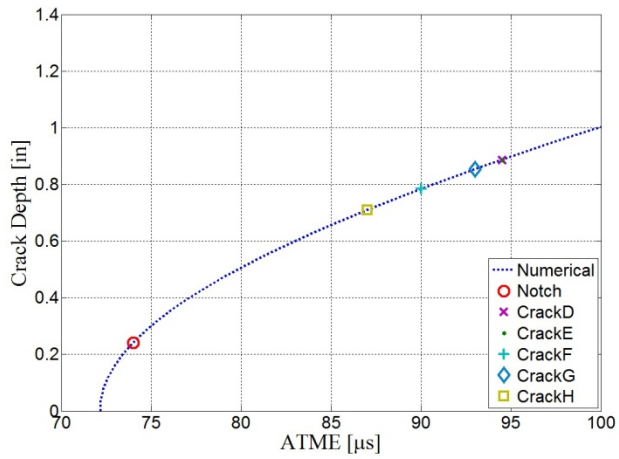


FIGURE 3.11

Crack depth estimation for Beam B

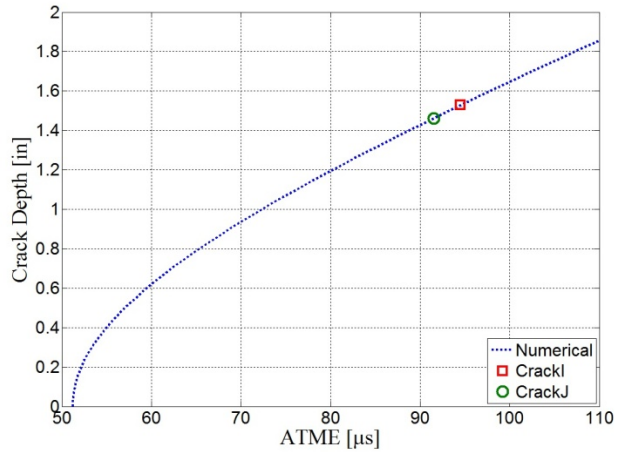


FIGURE 3.12

Crack depth estimation for Beam C

3.2.3 Destructive Test (Core Results)

To provide a more accurate ground truth measurement, dye is injected into the cracks and then a core is drilled containing the dye-injected crack. Dye is injected into crack D and H using an acetone-based dye forced into the crack with 0.06 ksi using the device shown



FIGURE 3.13

Dye injection apparatus

in FIGURE 3.13. The device is affixed to the concrete beam using a combination of metal/concrete 2-part epoxy and two bar clamps. The pressure is applied through the Schrader valve, seen at the top of the injection device, via a hand pump with a pressure indicator.

After dye was injected, a 2.5 in core is drilled to determine how deep the dye reached. Theoretically, the crack is the same depth throughout the cross section of the beam; however in practice, the crack depth varies across the cross section. To counteract this complication, the coring bit is positioned so that the outer edge of the core corresponds with the location, across the width of the beam, where the ultrasonic equipment was placed. This coring setup can be seen in FIGURE 3.14.

The results of these testing can be seen in FIGURE 3.15 and FIGURE 3.16. The visual inspection technique overestimates the crack depth when compared to the core result. Crack initiation tends to happen at imperfections and free surfaces, so a deeper

crack at the surface of the beam is to be expected. Finally, the diffusion method most closely estimates the crack depth according to the core result within 0.4 in variation.



FIGURE 3.14
Coring process

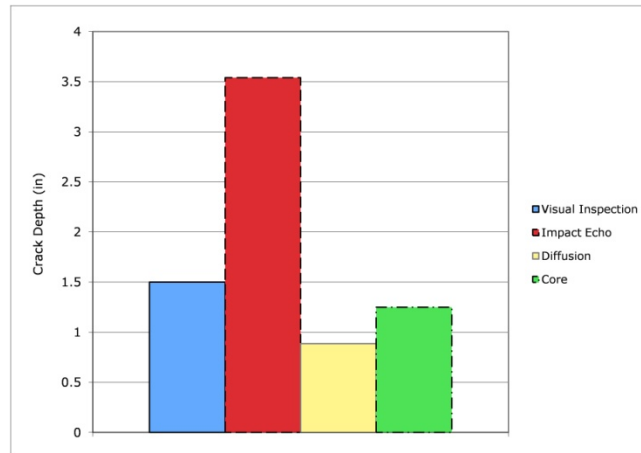


FIGURE 3.15
Comparison of depth measurement techniques to crack D

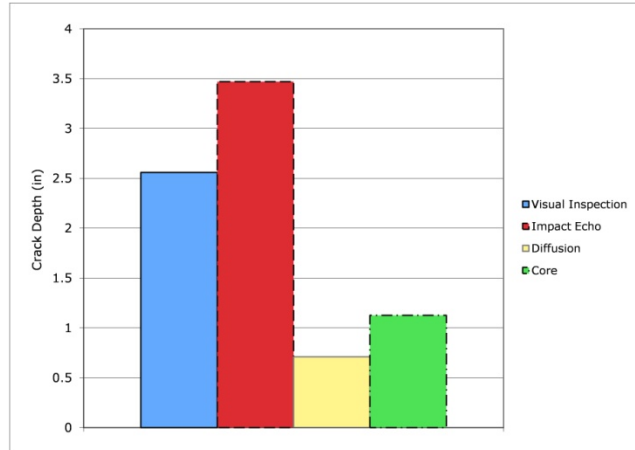


FIGURE 3.16

Comparison of depth measurement techniques to crack H

3.2.4 Comparisons and Summary of Results

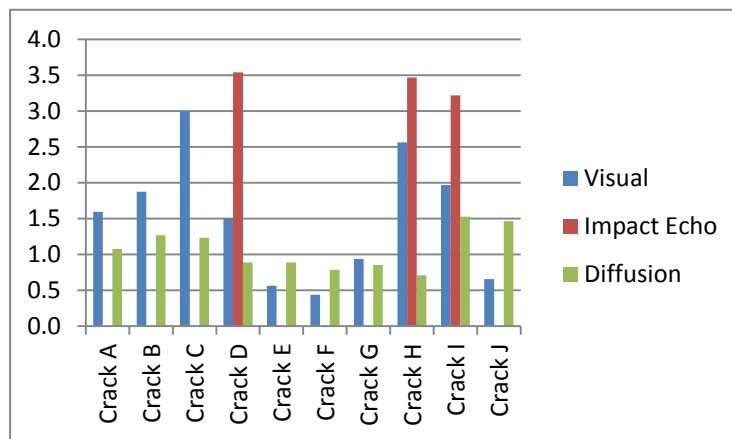
The results of these testing can be seen in TABLE 3.4 and FIGURE 3.17. The visual inspection technique overestimates the crack depth when compared to the core results. Crack initiation tends to happen at imperfections and free surfaces, so a deeper crack at the surface of the beam is to be expected. Finally, the diffusion method most closely estimates the crack depth according to the core result within the range of 0.4 in variation.

3.3 Summary

This research presents the diffuse ultrasonic technique that has been developed to estimate surface crack depth in concrete bridge elements. Findings of the research are summarized as follows:

TABLE 3.4**Comparison of depth measurement techniques to all cracks (inch)**

After Unloading	Visual	Impact Echo	Core	Diffusion
Crack A	1.59			1.074803
Crack B	1.88			1.267717
Crack C	3.00			1.232283
Crack D	1.50	3.54	1.25	0.887122
Crack E	0.56			0.887122
Crack F	0.44			0.783846
Crack G	0.94			0.853623
Crack H	2.56	3.47	1.13	0.709448
Crack I	1.97	3.22		1.528291
Crack J	0.66			1.462061

**FIGURE 3.17***Comparison of depth measurement techniques to all cracks (inch)*

First, the proposed and developed diffuse ultrasonic technique together with numerical simulation data base can estimate the depth of surface breaking cracks in concrete with an accuracy of ± 0.5 in. This was proved by comparing the actual crack depths that were measured from cores.

Second, the diffuse ultrasonic technique estimates crack depths more accurately than the impact echo technique and visual inspection (from the sides of the beam).

Third, the diffuse ultrasonic technique is little affected by crack geometry. This implies that the crack orientation cannot be determined with this method. However, it is shown from the numerical results that within a reasonable range of crack angles the diffuse ultrasonic estimation produces maximum errors less than 10%.

Fourth, for the reason mentioned in the above, the diffuse ultrasonic technique, as of today, appears to be superior to the other existing techniques such as impact echo or wave transmission technique.

4 Bridge Weigh-in-Motion (BWIM) Analysis

The work to date consisted of developing a BWIM algorithm to identify axle weights of moving vehicles varying with time history with the application of two-dimensional moving force identification (MFI) theory associated with dynamic programming method together with first-order Tikhonov regularization technique. An eigenvalue reduction technique is applied to reduce the dimension of the system, and the continuous equilibrium equation of motion is transformed into a discrete vector matrix differential equation suitable for dynamic programming method. Minimization of least-squares of the difference between measured strains and theoretical ones are applied for the inverse problem. Hansen's L-Curve method is employed to optimally estimate the smoothing parameter and the first-order Tikhonov regularization technique is also applied to obtain smoother result. The dynamic programming method is then used to provide an efficient solution to the recursive least squares formulation. The algorithm is based on sophisticated FE model of the bridge and implemented with the program written in MATLAB.

A FE model, which constitutes bending plate element and grillage beam element, is established to model the bridge and extract information for implementing the proposed MFI algorithm. The established FE model is verified by comparing the simulated strain data (from the FE model) with the measured ones (from the BWIM system) of passing vehicles from both shape and magnitude. Field testing of the bridge on highway US-78 in Alabama in the U.S. is applied to verify the proposed FE model and MFI algorithm, including two typical vehicles on the highway of static-known weight and dimensions (2-axle rigid truck and 5-axle semi-trailer).

In testing the proposed MFI algorithm of axle weight identification of passing vehicles over the instrumented bridge, three different sets of strain data of the same passing vehicle are applied as input measurements to test the application of the proposed MFI algorithm, including two sets of the simulated strain from established FE model with different sensor numbers and positions, and the measured strain data from the BWIM system, respectively. Finally, the algorithm is tested and evaluated by comparing the equivalently static measured axle loads with the predicted ones from MFI algorithm.

In addition, the MFI algorithm was verified by the repeated runs of the calibration vehicles during the initial calibration, and the results were compared with the static weights. The proposed MFI algorithm illustrates considerable potential to be the basis for a highly accurate BWIM system and broads the application of BWIM system in different bridges in the future.

4.1 Moving Force Identification (MFI) Method

When evaluating existing bridges, information based on the actual resistance and traffic load expected over the structure will result in more accurate and reliable evaluation of the safety of existing bridges. The actual live load data for heavy vehicles not only assist in making high-level maintenance decisions regarding the entire bridge inventory, but also provide valuable information to state highway agencies and substantially assist in the establishment of the planning, administration, and enforcement application.

An innovative bridge weigh-in-motion (BWIM) technique can provide accurate traffic load effect. The BWIM system we used herein replaces traditional ones with axle detector technology named like ‘nothing on the road (NOR)’ or ‘free of axle detector

(FAD)' [9]. The BWIM system uses instrumented bridge as a large sensor, and the transducers are mounted on the bottom flange of each girder to weigh axle weight and gross vehicle weight (GVW) of heavy trucks with the dynamic strain data collected as the sampling frequency of 512 Hz, and the additional transducers mounted underneath the bridge slab to induce signals of the passing vehicles so as to detect them and obtain silhouette of the vehicle, including axle spacing, speed and vehicle configuration [9].

Conventional BWIM is based on static equations that relate the strains measured on the bridge to the (static) weights of the axles that cause those strains. There is one equation for each scan of the sensors and the problem is one of minimizing the sum of squares of differences between measured and theoretical strains. This reduces to a system of simultaneous equations.

We developed a Moving Force Identification (MFI) approach. This uses dynamic equations of motion that relate the measured strain to the applied dynamic forces applied by the truck's axles. However, the concept is the same in that the problem reduces to one of minimizing the sum of squares of differences between measured and theoretical strains.

The process starts with the standard equation of motion:

$$[M]\{\ddot{y}\} + [C]\{\dot{y}\} + [K]\{y\} = [L]\{f\} \quad (4.1)$$

where $\{y\}$ are displacements and $[M]$, $[C]$ and $[K]$ are the mass, damping and stiffness matrices respectively. $[L]$ is the location matrix and $\{f\}$ is the vector of unknown applied axle forces. This system of differential equations is solved in 'state space', i.e., it is reduced from one 2nd order matrix differential equation to two 1st order ones by defining

a displacement/velocity vector: $\{X\} = \begin{Bmatrix} y \\ \dot{y} \end{Bmatrix}$ and converting the problem into a discrete time integration scheme of the form:

$$\{X\}_{j+1} = [F]\{X\}_j + [G]\{f\}_j \quad (4.2)$$

where j is the time step number and $[F]$ and $[G]$ are functions of the bridge geometry and mass. The vector, $\{X\}$ is a function of displacement and its derivative which in turn is related to strain, which will be measured. Eq. (4.2) relates $\{X\}$ at the next time step to its current value and the current value of $\{f\}$, the vector of applied forces. We refer to Eq. (4.2) as a Dynamic Programming approach. The inverse problem is to find the applied forces, $\{f\}$, for given strains (related to $\{X\}$). This will be done using a simple least squares approach, i.e., finding $\{f\}_j$ which minimizes the sum of squares of differences between the measured value for $\{X\}_{j+1}$ and the value given by Eq. (4.2).

The problem is highly ill conditioned and requires a numerical method – Tikhonov Regularization – to be solved. However, finding the full displacement time history is a big step forward for BWIM and has the potential to greatly improve accuracy.

4.2 Demonstration of the application of the MFI Method

4.2.1 Derivation of Element Stiffness Matrix and Mass Matrix

The proposed MFI algorithm is based on a sophisticated FE model of the testing bridge. A FE model, which constitutes bending plate element and grillage beam element, is established to model the bridge and extract information for implementing the proposed MFI algorithm. Field testing of the bridge on highway US-78 in Alabama in the U.S., with an innovative bridge weigh-in-motion (BWIM) system installed on the instrumented bridge, is applied to verify the proposed FE model and the MFI algorithm, including two

typical vehicles on the highway of static-known weight and dimensions (2-axle rigid truck and 5-axle semi-trailer). The established FE model is verified by comparing the simulated strain data (from the FE model) with the measured ones (from the BWIM system) of passing vehicles from both shape and magnitude. The mathematical equations are derived and the proposed MFI algorithm is implemented by computer program written in MATLAB. Based on the calibrated FE model, these two vehicles are applied as examples to test the proposed algorithm of axle weight identification of passing vehicles over the instrumented bridge. Three different sets of strain data of the same passing vehicle are applied as input measurements to test the application of the proposed MFI algorithm, including two sets of the simulated strain from established FE model with different sensor numbers and positions, and the measured strain data from the BWIM system, respectively. Finally, the algorithm is tested and evaluated by comparing the equivalently static measured axle loads with the predicted ones from the MFI algorithm.

4.2.2 Meshing of the Instrumented Bridge on Highway US-78

The dimension of the cross section of the instrumented bridge on highway US-78 is listed in FIGURE 4.1. The bridge has three diaphragms along the driving direction; one is in the middle position, and two on the end of the bridge. The beam elements are associated with corresponding plate elements according to their positions.

As the bridge deck is not a regular slab, we have to change the bridge deck to an equivalent section. The inertial moment and torsional constant are calculated based on equivalent section, which is a combined section of girder and bridge deck [10]. Considering the effect of bridge deck, the properties of diaphragm can also be calculated as equivalent section.

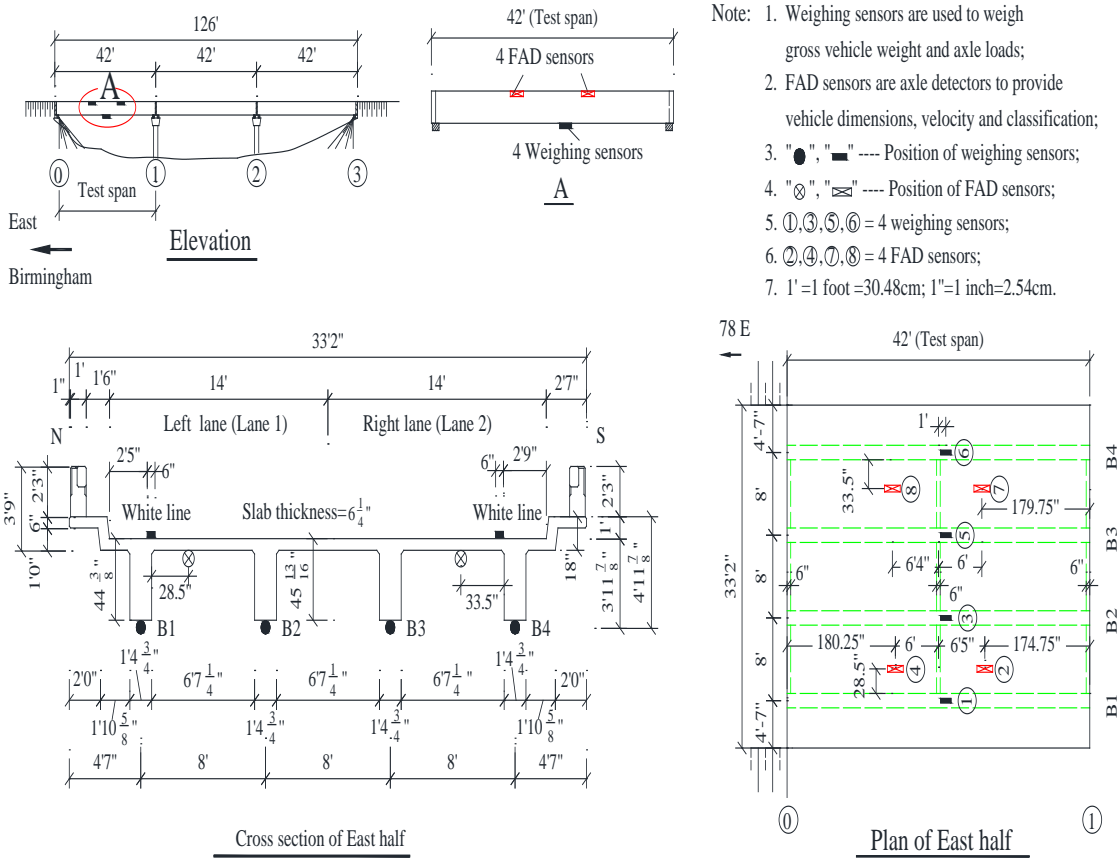


FIGURE 4.1

Dimension of the cross section

Along the driving direction, we mesh the deck with 28 elements with length 17.6 in. The width of the equivalent section is 360 in. Considering the position of main girder and the wheel loads, we mesh the deck along the transversal direction with 30 elements with length 12 in. The meshing of the bridge deck assures that the wheel loads are moving along the nodal lines. The aspect ratio of plate element is 1.46:1, which is in a reasonable range. The bridge model has 840 elements, 899 nodes and a total of 3596 DOFs.

4.2.3 Selection of Moving Vehicles

The bridge selected for the BWIM installation is located on the highway US-78 East in Graysville, Alabama, three miles west of highway I-22. The number of the bridge is BIN 7633. The bridge is smooth on the joint, and the approach to the bridge is even. The bridge is a three span simple supported T-beam bridge with span with two lanes in each direction. The information of the instrumented bridge is listed in FIGURE 4.1. In addition, the sensor position of the bridge is also illustrated in FIGURE 4.1. For the instrumentation of the BWIM system, the end span to the city of Birmingham direction was selected as test span (FIGURE 4.1). Four weighing sensors were mounted longitudinally on the soffit of concrete girders (one sensor for each girder) with one foot off the centre because of the diaphragm. To detect the vehicles and acquire the axle number of vehicle and axle spacing, four FAD sensors were mounted longitudinally underneath the concrete slab 12 feet apart for each separate lane.

The initial calibration test for the BWIM system was conducted. The initial calibration test was calibrated under the test condition (R1-I) according to the European specifications for BWIM [11]. The initial calibration was conducted with two semitrailers loaded to a capacity of 80,000 lbs from Alabama Department of Transportation (ALDOT) as pre-weighed trucks. During the initial calibration test, two pre-weighed trucks were running with different speeds at different lanes. Finally, we collected 10 repeated runs for each lane.

Calibration with random traffic is useful to get realistic information about the behavior of the BWIM system under real traffic flow and/or to recalibrate the BWIM system in actual traffic condition. The primary objective of testing is to determine the

accuracy of the BWIM system as compared to the static scales. Three specific days between November 2008 and February 2009 were scheduled for the in-service testing of the BWIM system.

Based on previous analysis, a FE model to simulate the whole process of vehicle passing the bridge is developed based on MATLAB. In order to check the model, we use one 2-axle vehicles (from in-serve testing) and one 5-axle vehicle (the calibration vehicle in the initial calibration) as examples, when they pass the bridge. The two vehicles drive along lane 2. The information of the vehicles is listed in TABLE 4.1.

4.2.4 Verification of the FE Model with Moving Vehicles

The section properties of the bridge components are based on previous calculation and design drawing. The material properties of the bridge (deck, beam and diaphragm) are determined just based on the design drawing. One method to check the bridge model is to make a comparison between the simulated frequencies and the measured ones. The other

TABLE 4.1
Vehicle information for model verification

Vehicle number	Item	Static axle weight (kips)					Axle spacing (in)			
		1st axle	2nd axle	3rd axle	4th axle	5th axle	A1-A2	A2-A3	A3-A4	A4-A5
1	Left wheel	6.34	13.34	/	/	/	228	/	/	/
	Right wheel	6.90	15.33	/	/	/	228	/	/	/
	Axle weight	13.23	28.66	/	/	/	Velocity = 947.4 in/s			
2	Left wheel	5.77	7.77	8.12	9.81	9.40	170	53	440	151
	Right wheel	5.52	8.23	8.33	8.79	8.99	170	53	440	151
	Axle weight	11.29	15.99	16.45	18.60	18.39	Velocity = 1066.9 in/s			

is to apply the corresponding result of static loading test to modify the parameters of the bridge. We did not carry out these two tests on bridge US-78; thus, we can only apply the dynamic strain data to check the model, from both magnitude and shape. According to the design drawing, the modulus of elasticity of girder is $E = 3190.83 \text{ ksi}$. In order to match the simulated strain data and the measured ones, the material of bridge deck and girders (including longitudinal girder and transversal diaphragms) are selected as follows.

For plate element:

$$E_x = E_y = 3190.83 \text{ ksi}, \nu_x = \nu_y = 0.2, \rho = 0.0867 \text{ lb/in}^3, G = 1450.4 \text{ ksi}$$

For all beam elements:

$$E = 3190.83 \text{ ksi}, \nu = 0.2, \rho = 0.0867 \text{ lb/in}^3, G = 1682.4 \text{ ksi}$$

During the simulation of the whole process from the moment that the first axle approaches the bridge to the moment that the last axle leave the bridge, the suspension of wheel loads are not taken into account because we do not have these related information. All the travelling wheel loads are simulated as constant force moving with constant velocity. During the calculation, we do not consider damping either.

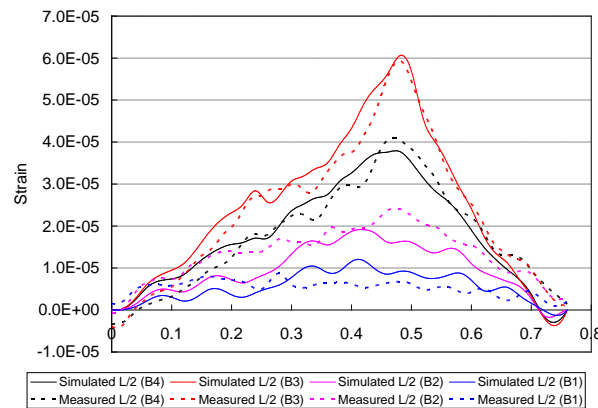


FIGURE 4.2

Strain comparison for vehicle 1

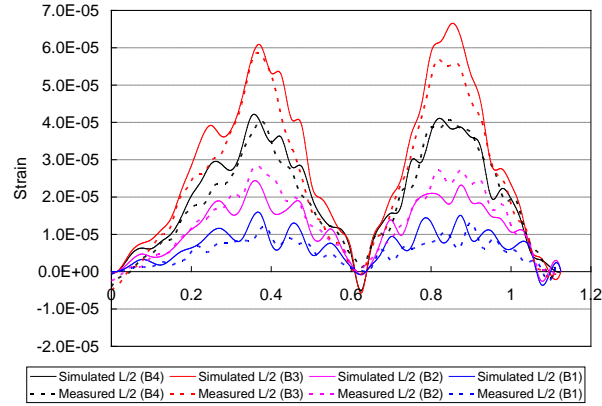


FIGURE 4.3

Strain comparison for vehicle 2

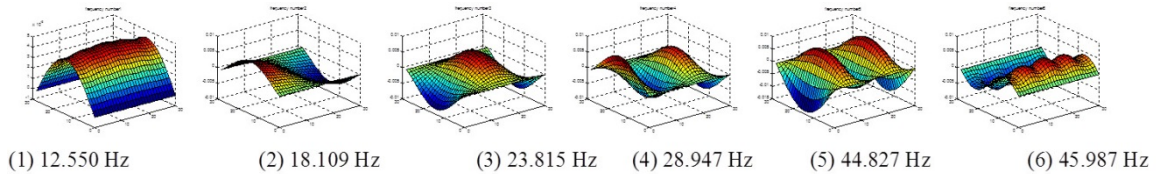


FIGURE 4.4

The first 6 mode shapes of the established FE bridge model

The measured strain data of all 4 sensors (mounted on the soffit of the mid span), which are acquired from the BWIM system, are compared with the simulated strain data from the established FE model and illustrated in FIGURE 4.2 and FIGURE 4.3 for vehicle 1 and 2, respectively. From FIGURE 4.2 and FIGURE 4.3, we can find that the simulated strain data, acquired from the modified bridge/vehicle FE model, and the corresponding measured ones match well in both shape and magnitude.

For this FE model, we conduct modal analysis. The first 6 modal shapes and corresponding frequencies are illustrated in FIGURE 4.4.

After we verify the efficiency of FE model of the bridge, we perform modal analysis of the FE model, because we need to select a finite number of modes to reduce

the order of bridge dynamic system of vibration in MFI algorithm associated with dynamic programming method and Tikhonov regularization method. Rowley (2007) demonstrates that the first 25 modes can provide sufficient accuracy in MFI with the application of first-order regularization technique [12]. In the following investigation, we consider 25 modes to reduce the order of dynamic system.

4.2.5 Field Testing of MFI with Full-Loaded 2-Axle Rigid Truck

For the slab-girder bridge, the critical section for mounting sensors are quarter span, mid span, and three fourth quarter span of the bridge. With the same FE model, when vehicle 1 passes the bridge, the simulated strain data of 4 longitudinal beams at three different positions ($L/4$, $L/2$, and $3L/4$) are illustrated in FIGURE 4.5.

If we mount sensors on the soffit of all girders on all sections ($L/4$, $L/2$, and $3L/4$), the number of sensors will be significantly increased; sometimes the number of sensors of the system may be not sufficient for wider bridge. This will lead to the limitation of the application of the BWIM system to wider bridge, especially for bridges with more than 6 girders.

In the general case, we just mount sensors on the soffit of mid span of the bridge.

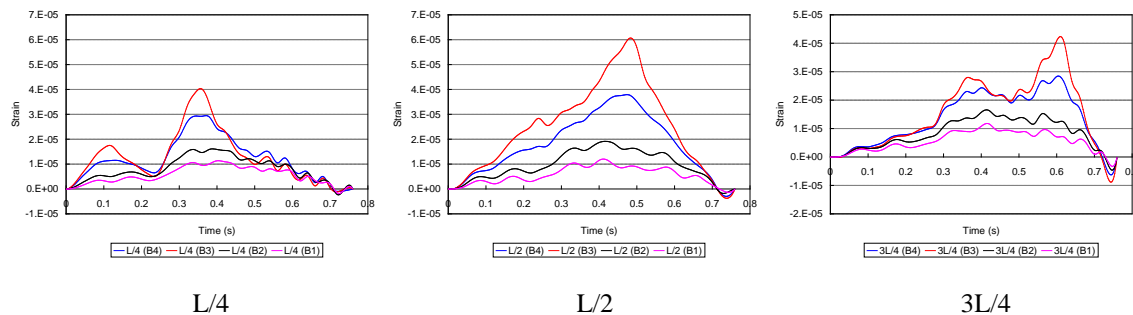


FIGURE 4.5

Simulated strain of full-loaded 2-axle vehicle

In order to check the algorithm for field testing application, the following three cases are investigated:

Case 1: We apply the simulated strain data of 12 measurement positions (on the soffit of four girders at L/4, L/2, and 3L/4), which are acquired from the developed MATLAB program, as the measured strain data to test the accuracy of MFI algorithm in wheel load and axle load identification.

Case 2: We employ measured strain of 4 measurement position (on the soffit of four girder at L/2), which are acquired from the BWIM system, as the input strain data.

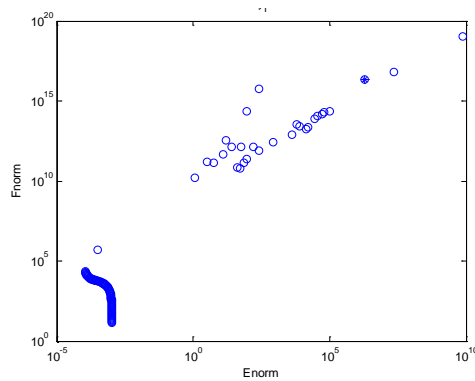


FIGURE 4.6

Relationship between E_{norm} and F_{norm}

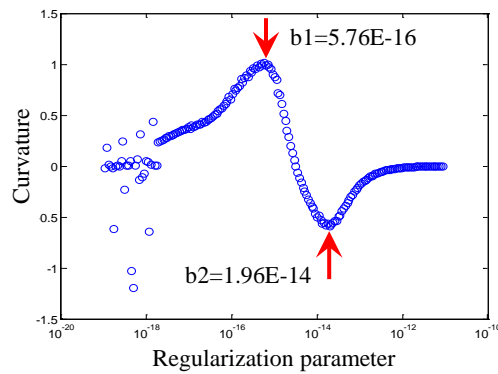


FIGURE 4.7

Relationship between regularization parameters

For case 1, we select 25 modes to reduce the order of the dynamic system, and 194 regularization parameters are selected in the range $10^{-19} \sim 10^{-11}$. The relationship between E_{norm} and F_{norm} are illustrated in FIGURE 4.6, and the relationship between regularization parameter and its corresponding curvature are listed in FIGURE 4.7.

From FIGURE 4.7, we can find two optimal regularization parameters, $b_1 = 5.76E-16$ and $b_2 = 1.96E-14$, the former is corresponding to the maximum positive curvature, and the latter the maximum negative curvature. In order to check which parameter will result in the better identification of moving wheel loads, we investigate the identified loads for both parameters, this paper just list the result of $b_1 = 5.76E-16$ in detail. With $b_1 = 5.76E-16$, the identified wheel loads are listed in FIGURE 4.8.

After we obtain the estimation of state variables vector $\{Y\}$ for each time step according to dynamic programming routine, we can calculate the estimation of strain data based on equation, $\{\varepsilon_i\} = [Q']\{Y\}$. Thus, we can compare the input strain data with the estimated ones. The comparison of those two series of strain data of different positions ($L/4$, $L/2$, and $3L/4$) are listed in FIGURE 4.9.

From FIGURE 4.8, we can see that the obtained smoothing parameter can provide an acceptable estimation of wheel loads for full-loaded 2-axle rigid truck. FIGURE 4.9 shows that with smaller regularization parameter, b_1 , estimation of strain data presents good match in comparison with input strain data.

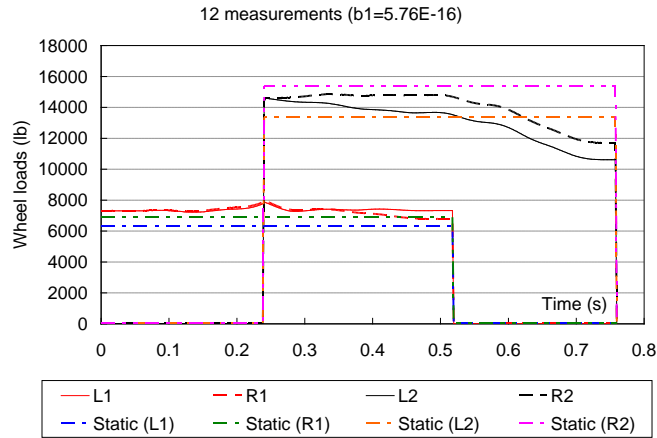


FIGURE 4.8

Identified wheel loads of 2-axle full-loaded rigid truck

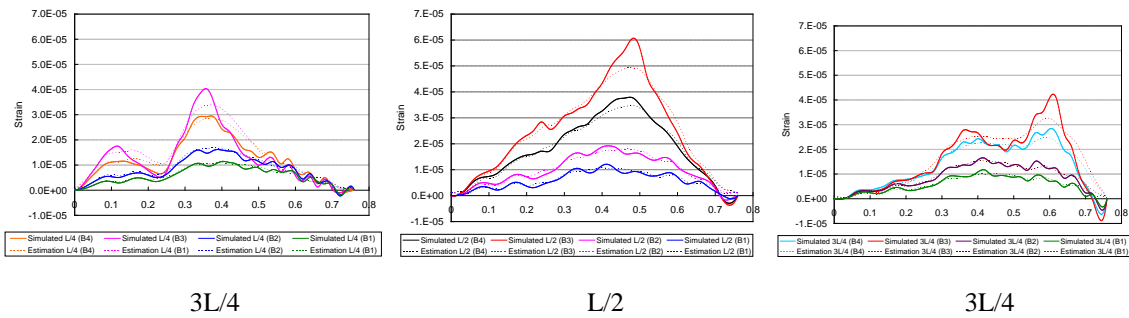


FIGURE 4.9

Comparison of strain data of 2-axle full-loaded rigid truck

For case (2), we also choose 194 regularization parameters in the range $10^{-19} \sim 10^{-11}$. The relationship between E_{norm} and F_{norm} are illustrated in FIGURE 4.10, and the relationship between regularization parameter and curvature is listed in FIGURE

4.11. From FIGURE 4.11, we can acquire the optimal regularization parameters,

$$b_1 = 1.67E - 16.$$

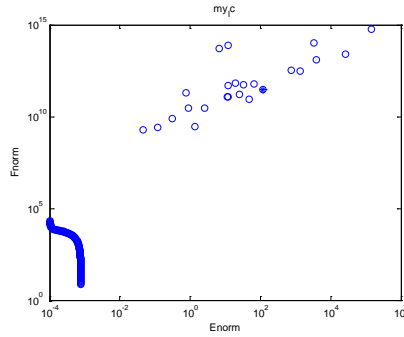
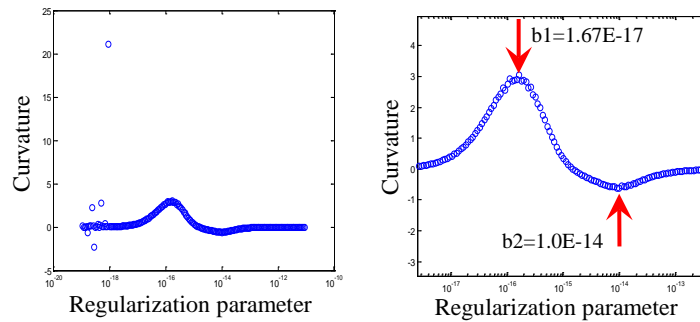


FIGURE 4.10

Relationship between curvature



(a) In a range of $10^{-19} \sim 10^{-11}$

(b) In a narrow range

FIGURE 4.11

Relationship between regularization parameters and E_{norm} and F_{norm}

When $b_1 = 1.67E - 16$, the identified wheel loads are listed in FIGURE 4.12. The comparison between simulated input strain data and estimated ones based on dynamic programming method at mid span is listed in FIGURE 4.13.

It is not possible to sufficiently evaluate the accuracy of MFI algorithm in the application of field testing according the case studies. On the one hand, we do not know the actual applied dynamic forces; on the other hand, the FE model may not sufficiently

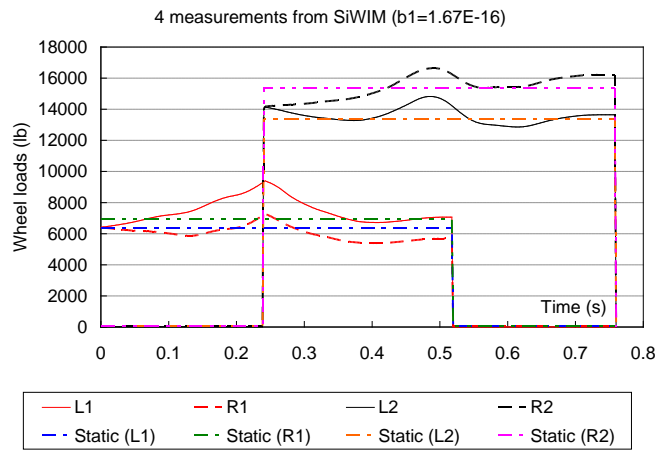


FIGURE 4.12

Identified wheel loads

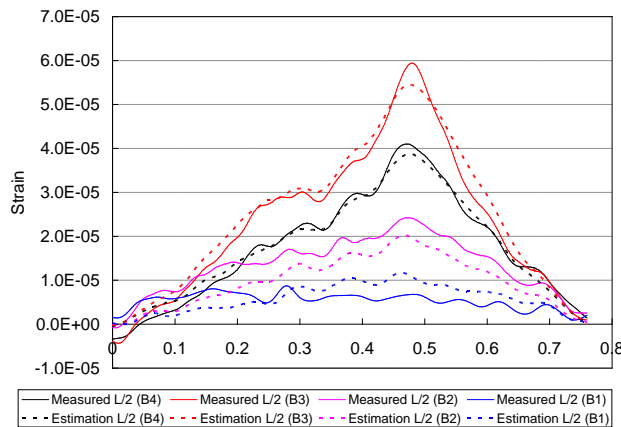


FIGURE 4.13

Comparison of strain data at L/2

represent the actual behavior of the bridge. However, for the above-mentioned two different cases, we can predict the axle weights and the GVW to be compared with static ones to verify the algorithm. Rowley (2007) demonstrates that the axle weights and the GVW can be acquired by averaging the identified forces in the middle 60% of the time history [12].

For comparison, we also investigate the case that 4 measurements of simulated strain data are as input strain (named as case 3). The optimal regularization parameters for this case is $b_1 = 6.43E - 17$. FIGURE 4.14 summarize the identified wheel loads for three different cases based on their own optimal regularization parameter b_1 .

From FIGURE 4.14, we find that the time history of identified moving forces is sensitive to the selected regularization parameter, the number of sensor positions, and the input strain data. Different numbers of sensor and different positions will result in significantly different results. At mid span, even the simulated strain data is quite similar to the measured ones, the time history of identified wheel loads for case 2 and 3 are quite different.

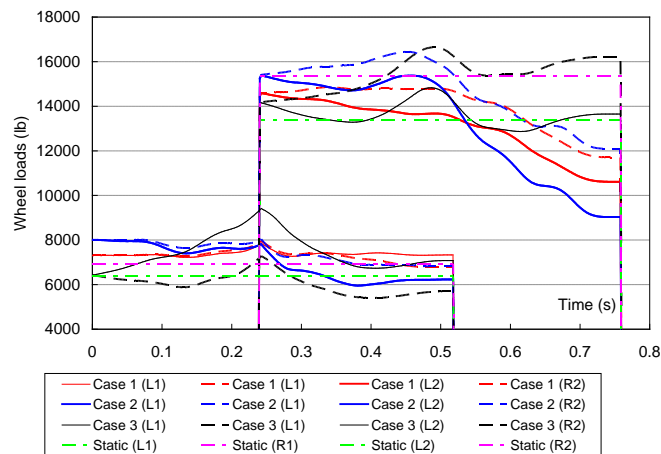


FIGURE 4.14

FIGURE 4.15 summarizes the identified axle loads for three different cases based on their own optimal regularization parameter b_1 , respectively. By averaging the identified forces in the middle 60% of time history, TABLE 4.2 illustrates the percentage error of identified wheel loads, axle loads, and GVW for three different cases with optimal regularization parameter in comparison with corresponding static loads. The calculated results with optimal regularization parameter b_2 are also listed in the table for

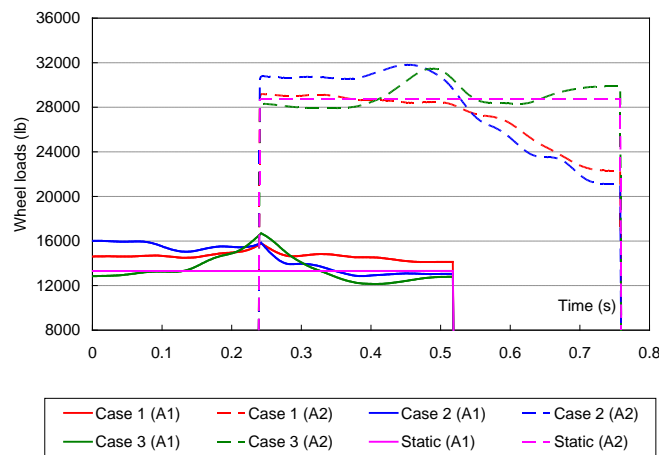


FIGURE 4.15

Identified axle loads for three cases

TABLE 4.2

Comparison of identified wheel and axle loads for full-loaded 2-axle truck (%)

Item	Case 1 - 12 simulated measurements		Case 2 - 4 simulated measurements		Case 3 - 4 measurements from the BWIM system	
	$b_1 =$	$b_2 =$	$b_1 =$	$b_2 =$	$b_1 =$	$b_2 =$
	$5.76E-16$	$1.96E-14$	$6.43E-17$	$1.0E-14$	$1.67E-16$	$1.0E-14$
L1	16.6	28.5	9.7	33.4	23.7	25.2
R1	7.2	17.7	7.9	19.8	-11.7	11.1
L2	-0.3	2.6	2.0	7.2	1.8	8.6
R2	-6.4	-10.3	-1.4	-5.9	1.4	-4.6
A1	11.7	22.8	8.8	26.3	5.3	17.8
A2	-3.5	-4.3	0.2	0.2	1.6	1.5

comparison.

From TABLE 4.2, we find the identified forces in case 1 are slightly better than case 2 and 3, because we use strain data of different sections ($L/4$, $2/L$, and $3L/4$) as input in case 1, while in case 2 and 3 we just use strain data at $L/2$ as input. We also find that for three different cases, smaller regularization parameter (b1) will result in better accuracy than larger regularization parameter (b2) in the identification of moving vehicles. The MFI algorithm can provide significantly satisfactory accuracy (within 3% in comparison with static results) for GVW if we select regularization parameter (b1) for three cases. For the axle weight identification, the accuracy is also acceptable (within 12%).

4.2.6 Field Testing of MFI with Full-Loaded 5-Axle Semitrailer

As the representative heavy vehicles on highways is semi-trailer or trailer, it is necessary to verify the algorithm with full-loaded 5-axle semi-trailer. In this case, we apply vehicle 2 in TABLE 4.1 as an example, which is the calibration vehicle for the initial calibration test. When vehicle 2 passes the bridge, the simulated strain data of 4 longitudinal beams at three different positions ($L/4$, $L/2$, and $3L/4$) are illustrated in FIGURE 4.16. Similar as the calculation in 2-axle rigid truck, we check three cases to verify the MFI algorithm.

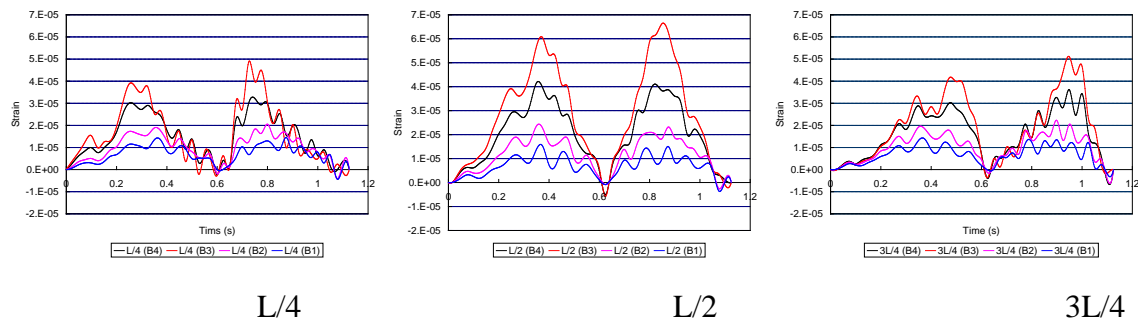


FIGURE 4.16

Simulated strain of full-loaded 5-axle semi-trailer

Case 1: 12 measurements of simulated strain data as input strain – The relationship between E_{norm} and F_{norm} are illustrated in FIGURE 4.17, and the relationship between regularization parameter and its corresponding curvature are listed in FIGURE 4.18. From FIGURE 4.18, we can find two optimal regularization parameters, $b_1 = 3.35E-16$ and $b_2 = 3.25E-14$.

When $b_1 = 3.35E-16$, the identified wheel loads are listed in FIGURE 4.19. From FIGURE 4.19, it is found that the identification of wheel loads for 5-axle vehicle illustrate unsatisfactory results for group axles, say, the axles have closed spacing (axle 2

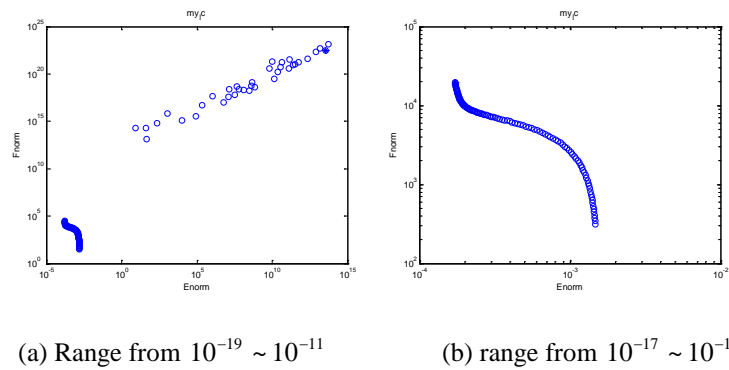


FIGURE 4.17

Relationship between E_{norm} and F_{norm} parameters and curvature

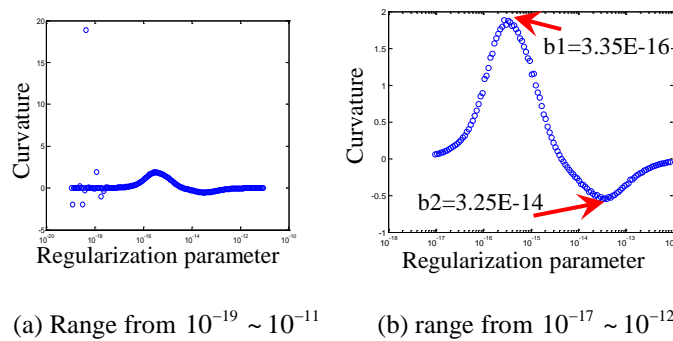


FIGURE 4.18

Comparison of strain data at L/2 Relationship between regularization

and 3; axle 4 and 5 for this semi-trailer). Then we sum the close-spaced group wheel loads together; FIGURE 4.20 lists the identified single wheel loads and group wheel loads. The comparison between simulated input strain data and estimated ones at different positions (L/4, L/2, and 3L/4) are listed in FIGURE 4.21.

From FIGURE 4.20, the optimal regularization parameter illustrates reliable estimation of single wheel loads and group wheel loads for full-loaded 5-axle semitrailer. The estimation of two group axles is close to the static loads.

Case 2: 4 measurements of simulated strain data as input strain – Case 2 is also investigated for comparison, and we can find two optimal regularization parameters,

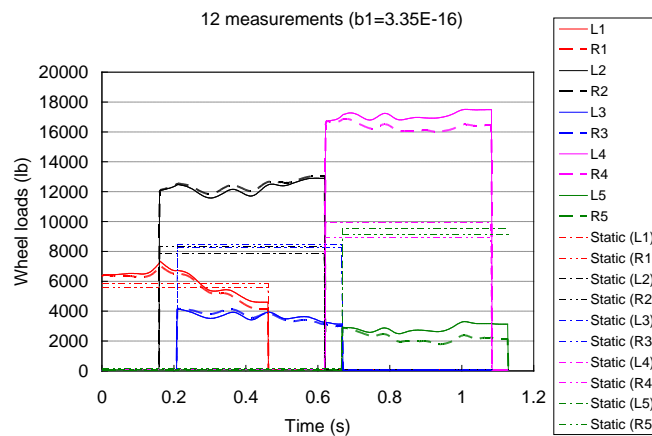
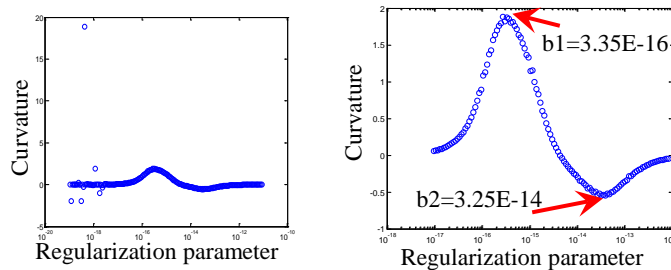


FIGURE 4.19

Identified wheel loads for 5-axle semi-trailer



(a) Range from $10^{-19} \sim 10^{-11}$

(b) range from $10^{-17} \sim 10^{-12}$

FIGURE 4.20

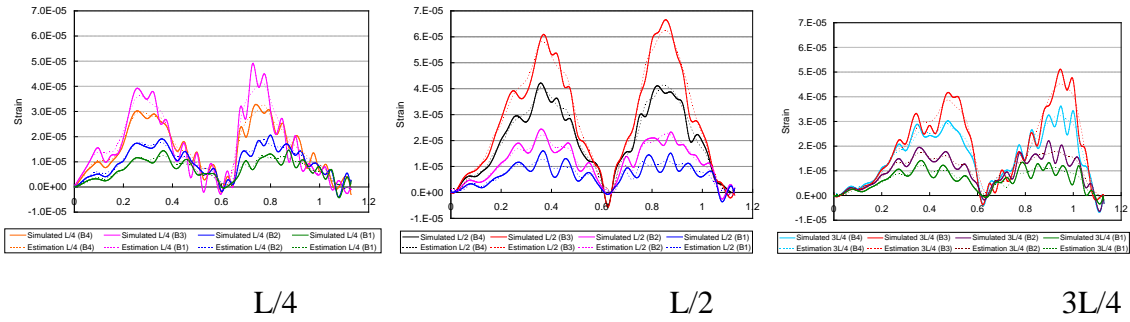


FIGURE 4.21

Comparison of strain data of full-loaded 5-axle semi-trailer at different position

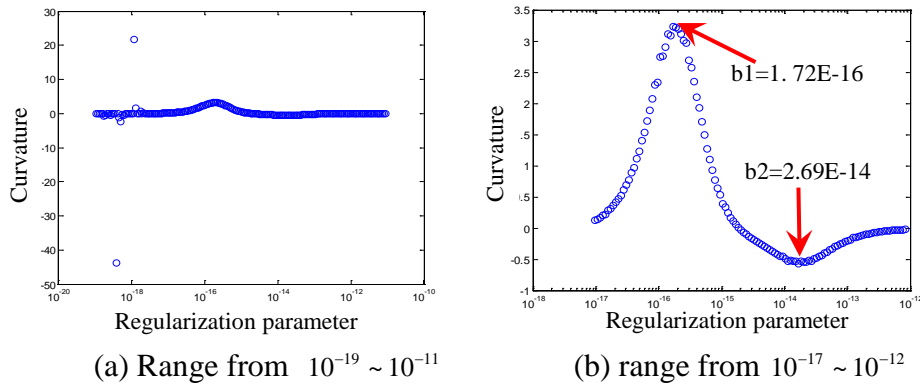


FIGURE 4.22

Relationship between regularization parameters and curvature of full-loaded 5-axle semi-trailer

$b_1 = 1.07E - 16$ and $b_2 = 1.67E - 14$. However, only the final identified wheel loads and axle loads are listed in the following TABLE 4.3.

Case 3: 4 measurements of measured strain data from the BWIM system as input strain – The relationship between regularization parameter and its corresponding curvature are listed in FIGURE 4.22. From FIGURE 4.22, we can find the corresponding optimal regularization parameters are $b_1 = 1.72E - 16$ and $b_2 = 2.69E - 14$.

When $b_1 = 1.72E - 16$, the identified single wheel loads and group wheel loads are listed in FIGURE 4.23. The comparison between simulated input strain data and estimated ones at mid span is listed in FIGURE 4.24.

FIGURE 4.25 summarizes the identified single and group wheel loads for three different cases based on their own optimal regularization parameter b_1 . FIGURE 4.26 illustrates the identified single and group axle loads for three different cases based on

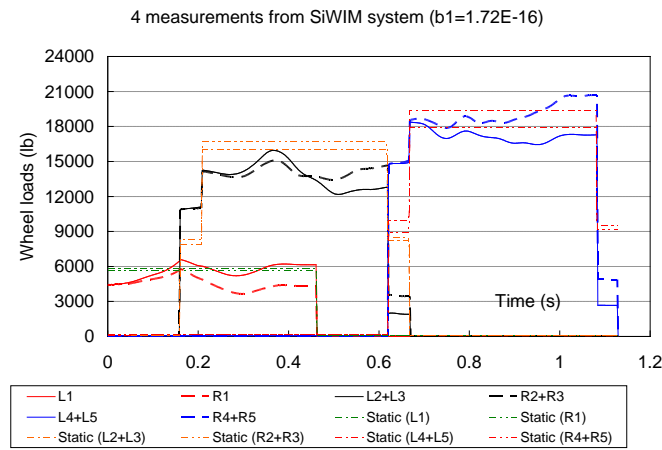


FIGURE 4.23

Identified single and group wheel loads

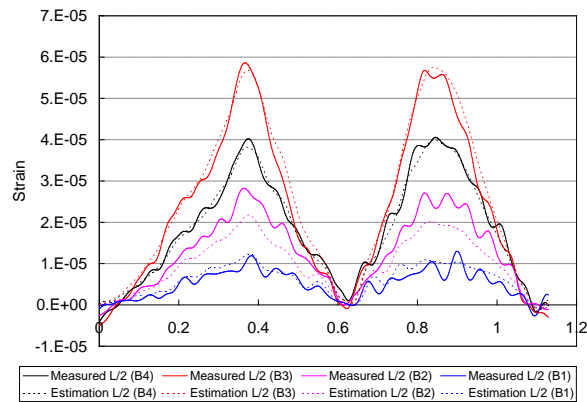


FIGURE 4.24

Comparison of strain data at L/2

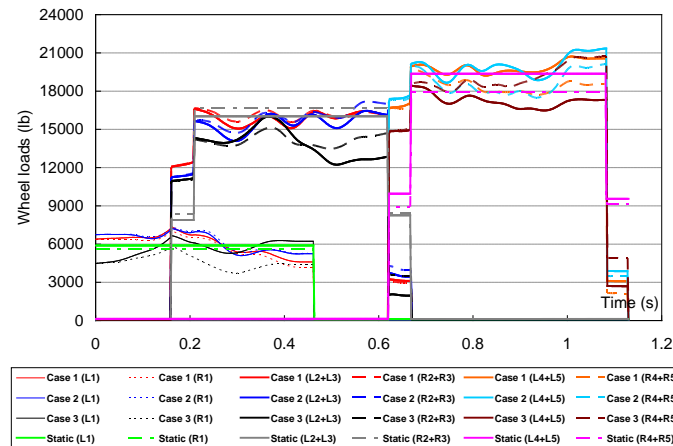


FIGURE 4.25

Identified single and group wheel loads for three cases

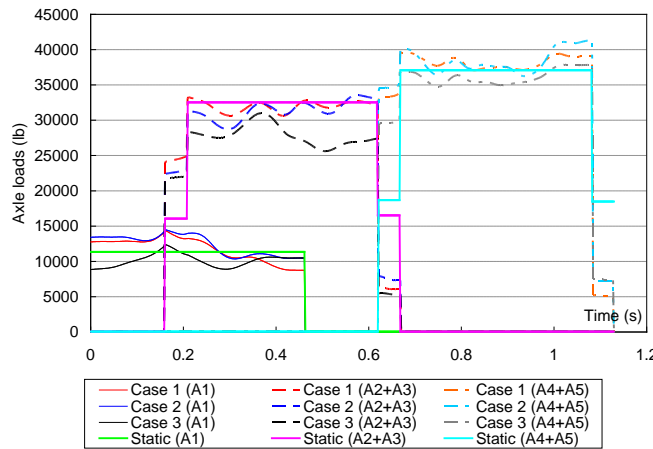


FIGURE 4.26

Identified single and group axle loads for three cases

their own optimal parameter b_1 .

From FIGURE 4.25 and FIGURE 4.26, the MFI algorithm illustrates acceptable estimation of single and group wheel loads for 5-axle semitrailer for all three cases. Case 1 and 2 depicts a better accuracy than case 3 in terms of time history. This demonstrates that we should modify the FE model to sufficiently represent the actual behavior of the

bridge, if we want to acquire better accuracy for the application of MFI algorithm in field testing.

By averaging the identified forces in the middle 60% of time history, TABLE 4.3 summarizes the percentage error of the identified wheel loads, axle loads, and GVW for three different cases with different regularization parameter, in comparison with corresponding static loads.

From TABLE 4.3, we can find when we apply MFI algorithm for axle forces identification for 5-axle semi-trailer, the sum of these group axles can predict reasonable results in comparison with static results. When we apply simulated strain data as input (case 1 and 2) and select the regularization parameter (b_1), which is corresponding to the maximum positive curvature, the MFI algorithm can achieve particularly accurate estimation of GVW (within 2% in comparison with static results) and GOA (within 5%); for single axle (SA), the algorithm also provide acceptable accuracy (within 11%). With

TABLE 4.3
Comparison of identified single and group loads for full-loaded 5-axle semi-trailer (%)

Item	Case 1 - 12 simulated measurements		Case 2 - 4 simulated measurements		Case 3 - 4 measurements from the BWIM system	
	$b_1 =$	$b_2 =$	$b_1 =$	$b_2 =$	$b_1 =$	$b_2 =$
	$3.35E-16$	$3.25E-14$	$1.07E-16$	$1.67E-14$	$1.72E-16$	$2.69E-14$
L1	7.8	20.0	7.2	27.4	-0.8	-6.4
R1	8.8	24.7	14.9	31.4	-17.7	-4.1
L2+L3	-1.6	-2.4	-3.8	-4.0	-12.8	-11.2
R2+R3	-3.9	-6.3	-5.0	-7.6	-15.6	-14.7
L4+L5	2.4	-1.1	2.5	-1.4	-12.2	-7.3
R4+R5	2.0	6.4	2.2	6.0	5.6	0.4
A1	8.3	22.3	10.9	29.3	-9.1	-5.2
A2+A3	-2.7	-4.4	-4.4	-5.8	-14.2	-13.0
A4+A5	2.2	2.5	2.4	2.2	-3.6	-3.6
GVW	1.1	2.5	0.8	2.7	-8.6	-7.6

the measured strain data as input, estimation of GVW, GOA, and SA is within 9%, 15%, 10%, respectively in comparison with static results.

4.3 Summary

Two case studies of a 2-axle rigid truck and a 5-axle semitrailer from field test on bridge on highway US-78 in Alabama demonstrates that the proposed MFI algorithm can provide an acceptable estimation of wheel loads and axle ones of moving heavy vehicles in comparison with static results, with the field bridge instrumented with the latest BWIM system.

The proposed MFI algorithm is based on a sophisticated FE model of the testing bridge. With the comparison between the simulated strain data based on the established FE model and the measured ones as input, the time history of identified moving forces demonstrates that the proposed MFI algorithm is sensitive to the selected regularization parameter, the number and position of sensors, and the input strain data. The investigation of three different cases (12 measurements from simulated strain, 4 measurements from simulated strain, and 4 measured strain data) demonstrates that during field testing, if we just mount sensors on soffit of each girder at mid span section of slab-girder bridge, the proposed MFI algorithm has sufficient accuracy in identifying wheel loads and axle loads. It is not necessary to mount sensors on all critical sections ($L/4$, $2/L$, and $3L/4$). When we apply the simulated strain data from the established FE model, we can achieve a better estimation of the identified axle loads in comparison with that from measured strain by the BWIM system. This demonstrates that we should

modify the FE model to more accurately represent the actual behavior of the bridge, if we want to acquire better accuracy for the application of MFI algorithm in field testing.

L-curve method is an effective tool to identify the optimal regularization parameter for the dynamic programming method in the application of MFI theory, however, the relationship between the regularization parameters and their corresponding curvature can more conveniently point the optimal regularization parameters which is corresponding to the maximum curvature.

After we average the identified forces in the middle 60% of the time history, we can acquire the averaged forces and make a comparison with static results. Case study of a 2-axle rigid truck shows that the MFI algorithm can achieve remarkably satisfactory accuracy for GVW (within 3% in comparison with the actual static weight) if we select the optimal regularization parameter for all three different cases. For the axle weight identification, the accuracy is also acceptable (within 12% in comparison with the actual static weight).

Case study of 5-axle semi-trailer shows that both the individual axle loads and the sum of group axles can be predicted with reasonable accuracy in comparison with static results. When we apply simulated strain data as input (case 1 and 2) and select the regularization parameter (b1), the MFI algorithm can achieve significantly accurate estimation of GVW (within 2% in comparison with the actual static weight) and GOA (within 5%); for SA, the algorithm also provide satisfactory accuracy (within 10%). With the measured strain data as input (case 3), estimation of GVW, GOA, and SA is also satisfactory, even it is less accurate than that from the simulated strain data as input. The

error of identified GVW, GOA, and SA in comparison with static results is within 10%, 15%, and 10%, respectively.

The investigation of all two typical vehicles illustrates that the MFI algorithm can achieve an exceptionally reasonable estimation of GVW (within 3% in comparison with static results) for slab-girder bridge if we select appropriate regularization parameter and employ the simulated strain data as input. The research demonstrates that the MFI algorithm, associated with dynamic programming method together with first-order Tikhonov regularization technique, can be applied in field testing if we can modify our bridge model to accurately represent the actual behavior of the bridge.

The proposed MFI algorithm demonstrates a potential tool in identifying axle loads of moving heavy vehicles which illustrates considerable potential to be the basis for a highly accurate BWIM system, can be employed for enforcement prescreening and control of oversized and overweight vehicles to prevent the existing bridges from deteriorated damage.

5 Summary and Discussion

Investigators in this project have developed a wireless BWIM+NDE system to assist in monitoring transportation infrastructure safety, for the first time ever, in a two-fold approach: control of overloaded trucks and safety assessment/monitoring of transportation infrastructure. The system contains individual wireless sensing nodes that integrate state-of-the-art ultrasonic nondestructive evaluation (NDE) devices suitable for crack growth monitoring, as well as wireless strain sensors for bridge weigh-in-motion (BWIM) analysis. The result is a transportation infrastructure monitoring and protection system that is highly portable, effective, where the installation and operation requires little manpower.

Based upon previous proof-of-concept devices, the researchers developed a compact wireless sensing node with sophisticated functionalities supporting strain gages, ultrasonic NDE transducers, accelerometers, etc. Latest off-the-shelf components are adopted to serve as key components in the wireless sensing node, including microprocessor, wireless transceiver, and analog-to-digital converter. Necessary signal-conditioning circuitries have been designed to interface the sensing node with various BWIM strain gages and ultrasonic transceivers. Solar panel can provide sustainable power supplies to both wireless sensors and a local gateway that collects data onsite from wireless sensors. Through cell phone data network, the gateway pushes data to be accessible online.

In addition, the researchers have developed the diffuse ultrasonic technique for estimating surface crack depth in concrete bridge. The proposed and developed diffuse

ultrasonic technique together with numerical simulation data base can estimate the depth of surface breaking cracks in concrete with an accuracy of ± 0.5 in. The diffuse ultrasonic technique estimates crack depths more accurately than the impact echo technique and visual inspection (from the sides of the beam). It is shown from the numerical results that within a reasonable range of crack angles the diffuse ultrasonic estimation produces maximum errors less than 10 %. The diffuse ultrasonic technique, as of today, appears to be superior to the other existing techniques such as impact echo or wave transmission technique.

Towards BWIM, our research focuses on developing a new algorithm utilizing the Moving Force Identification (MFI) approach. MFI is a method of solving the complex dynamic system that contains the interaction between a vibrating bridge and a moving truck, while the truck bounces and rocks over the bridge. The investigation of all two typical vehicles illustrates that the MFI algorithm can achieve an exceptionally reasonable estimation of vehicle weight (within 3% in comparison with static results) for a slab-girder bridge if we select appropriate regularization parameter and employ the simulated strain data as input. The research demonstrates that the MFI algorithm, associated with dynamic programming method together with first-order Tikhonov regularization technique, can be applied in field testing if we can modify our bridge model to accurately represent the actual behavior of the bridge. The proposed MFI algorithm demonstrates a potential tool in identifying axle loads of moving heavy vehicles which illustrates considerable potential to be the basis for a highly accurate BWIM system, can be employed for enforcement prescreening and control of oversized and overweight vehicles to prevent the existing bridges from deteriorated damage.

6 Bibliography

- [1] T. Cooklev, *Wireless Communication Standards : a Study of IEEE 802.11, 802.15, and 802.16*. New York: Standards Information Network IEEE Press, 2004.
- [2] M. Kane, D. Zhu, M. Hirose, X. Dong, B. Winter, M. Häckell, J. P. Lynch, Y. Wang, and A. Swartz (Eds.), *Development of an Extensible Dual-Core Wireless Sensing Node for Cyber-Physical Systems in Proceedings of SPIE, Sensors and Smart Structures Technologies for Civil, Mechanical, and Aerospace Systems*, San Diego, CA, USA, 2014.
- [3] J. H. Page, H. P. Schriemer, A. E. Bailey, and D. A. Weitz, "Experimental test of the diffusion approximation for multiply scattered sound," *Physical Review E (Statistical Physics, Plasmas, Fluids, and Related Interdisciplinary Topics)*, vol. 52, pp. 3106-3114, 1995.
- [4] R. L. Weaver, "Ultrasonics in an aluminum foam," *Ultrasonics*, vol. 36, pp. 435-442, 1998.
- [5] M. Seher, C.-W. In, J.-Y. Kim, K. E. Kurtis, and L. J. Jacobs, "Numerical and experimental study of crack depth measurement in concrete using diffuse ultrasound," *Journal of Nondestructive Evaluation*, vol. 32, pp. 81-92, 2013.
- [6] M. Seher, C.-W. In, J.-Y. Kim, K. E. Kurtis, and L. J. Jacobs, "Numerical and Experimental Study of Crack Depth Measurement in Concrete Using Diffuse Ultrasound," *J Nondestruct Eval*, 2012.
- [7] M. Seher, *Finite element simulation of crack depth measurements in concrete using diffuse ultrasound*, Master Dissertation, Civil and Environmental Engineering, Georgia Institute of Technology. Atlanta, 2011.

- [8] P. Anugonda, J. S. Wiehn, and J. A. Turner, "Diffusion of ultrasound in concrete," *Ultrasonics*, vol. 39, pp. 429-435, 2001.
- [9] C. ZAG, *SiWIM Bridge Weigh-in-Motion Manual*. Slovenia, 2005.
- [10] E. J. O'Brien and D. L. Keogh, *Bridge deck analysis*. London and new York: Taylor & Fransis Group, 2000.
- [11] C. 323, *European Specification on Weigh-in-Motion of Road Vehicles*, LCPC, Paris, Final Report, Appendix I, Ver. 3.0, EUCO-COST/323/8/99, 1999.
- [12] C. W. Rowley, *Moving force identification of axle forces on bridges*, *PhD dissertation*, Dissertation, UCD School of Architecture Landscape & Civil Engineering, University College Dublin, National University of Ireland, 2007.